

# Hydrothermal evolution and isotope studies of the Baghu intrusion-related gold deposit, Semnan province, north-central Iran



Shojaeddin Niroomand<sup>a,\*</sup>, Jamshid Hassanzadeh<sup>b</sup>, Hossein Ali Tajeddin<sup>c</sup>, Sina Asadi<sup>d</sup>

<sup>a</sup> School of Geology, College of Science, University of Tehran, Tehran, Iran

<sup>b</sup> Division of Geological and Planetary Sciences, California Institute of Technology, Pasadena, CA, USA

<sup>c</sup> Department of Geology, Faculty of Basic Sciences, Tarbiat Modarres University, Tehran, Iran

<sup>d</sup> Department of Earth Sciences, Faculty of Sciences, Shiraz University, Shiraz 71454, Iran

## ARTICLE INFO

### Keywords:

Intrusion-related gold systems  
Fluid inclusions  
Zircon U-Pb age  
Ar-Ar dating  
Stable isotopes  
Baghu  
Torud-Chahshirin Arc  
Central Iran

## ABSTRACT

The middle Eocene intrusion-related Baghu gold deposit is located in the Torud-Chahshirin segment of the Neotethyan magmatic arc of north-central Iran, Semnan province, Iran. The wallrocks at the deposit include a volcano-sedimentary sequence of calc-alkaline andesitic to dacitic lavas, marls, tuffs, and sandstones, which are intruded by epizonal granodioritic stocks and mafic dikes. Zircon U-Pb secondary ion mass spectrometry dating of a number of the granodiorite and micro-granite bodies yields an age of ca.  $43.4 \pm 1.3$  Ma. Mineralization is in the form of subparallel sheeted quartz veins that are up to ~1 km long within extensional faults. The ore-forming process included early potassic alteration with quartz + adularia + biotite + pyrite + chalcopyrite + native gold veins (average 0.25 g/t), and late phyllic alteration with quartz + sericite + pyrite + chalcopyrite + bornite + sphalerite + native gold veins (average 1.5 g/t). Supergene kaolinitization is also extensive in the Baghu area and has locally replaced up to 50 percent of the hypogene sulfide minerals. Turquoise is a diagnostic supergene phase, and locally, the iron oxy-hydroxides replacing the sulfides contain up to 57 g/t Au. The current hypogene and supergene resource estimate for the Baghu Au-Cu deposit is approximately 3.5 million tonnes averaging 1.17 g/t Au.

Fluid inclusions in quartz from phyllic stage vein samples include monophasic aqueous (I), monophasic gas-rich (II), aqueous liquid + vapor (III), mixed aqueous-carbonic (IV), and multi-solid (V) inclusion types. The average homogenization temperatures and salinities of fluid inclusion assemblages from type III and IV inclusions range from 180 to 382 °C, with a mode at about 330 °C, and 4.2–5.4 wt% NaCl equiv., respectively. The type IV inclusions showed clathrate melting temperatures between +3.1 and +8.5 °C, indicating salinities of 2.8–11.5 wt% NaCl equiv. The type V inclusions also show a  $T_h$  range from 310 to 478 °C (average 440 °C) corresponding to high salinities of 33–45 wt% NaCl equiv. The trapping pressure of the fluid inclusions was estimated to be 94–132 MPa corresponding to depths of 2.5–3.9 km during late stage of mineralization. Sericite from the stage II veins yields an  $^{40}\text{Ar}/^{39}\text{Ar}$  age of ca. 44 Ma, suggesting that the mineralization at Baghu overlap granite emplacement. The  $\delta^{18}\text{O}$  of the ore-forming fluid also indicates no significant meteoric water input, despite gold deposition in a relatively shallow epizonal environment ( $\delta^{18}\text{O}_{\text{fluid}} = +8.0$  to  $+10.3$  per mil). In addition,  $\delta^{34}\text{S}$  values in stage II pyrite and chalcopyrite sulfide minerals range from +1.5 to +3.1 per mil, which is consistent with fluid saturation from a reduced magmatic source of sulfur. Historic gold production from occurrences hosted by the Torud-Chahshirin volcano-plutonic complex has been minor compared to that from orogenic gold deposits in Iran. However, identification of intrusion-related gold deposits in the complex indicates that more thorough exploration in the Eocene arc of north-central Iran could be promising.

## 1. Introduction

Magmatic-hydrothermal systems above active subduction zones are important sources of gold. These ore deposits are usually in close spatial and temporal association with epizonal, intermediate to felsic, medium-

to high-K calc-alkaline igneous rocks (Sillitoe, 2008). Because of such close igneous connection, examining of the ore forming processes requires a special attention to the initial oxidation state of the causative magmas (Hart et al., 2004, 2005). Ishihara (1977, 1981, 2004) categorized granitoids into magnetite (I-type; oxidized) and ilmenite (S-

\* Corresponding author.

E-mail address: [niroomand@ut.ac.ir](mailto:niroomand@ut.ac.ir) (S. Niroomand).

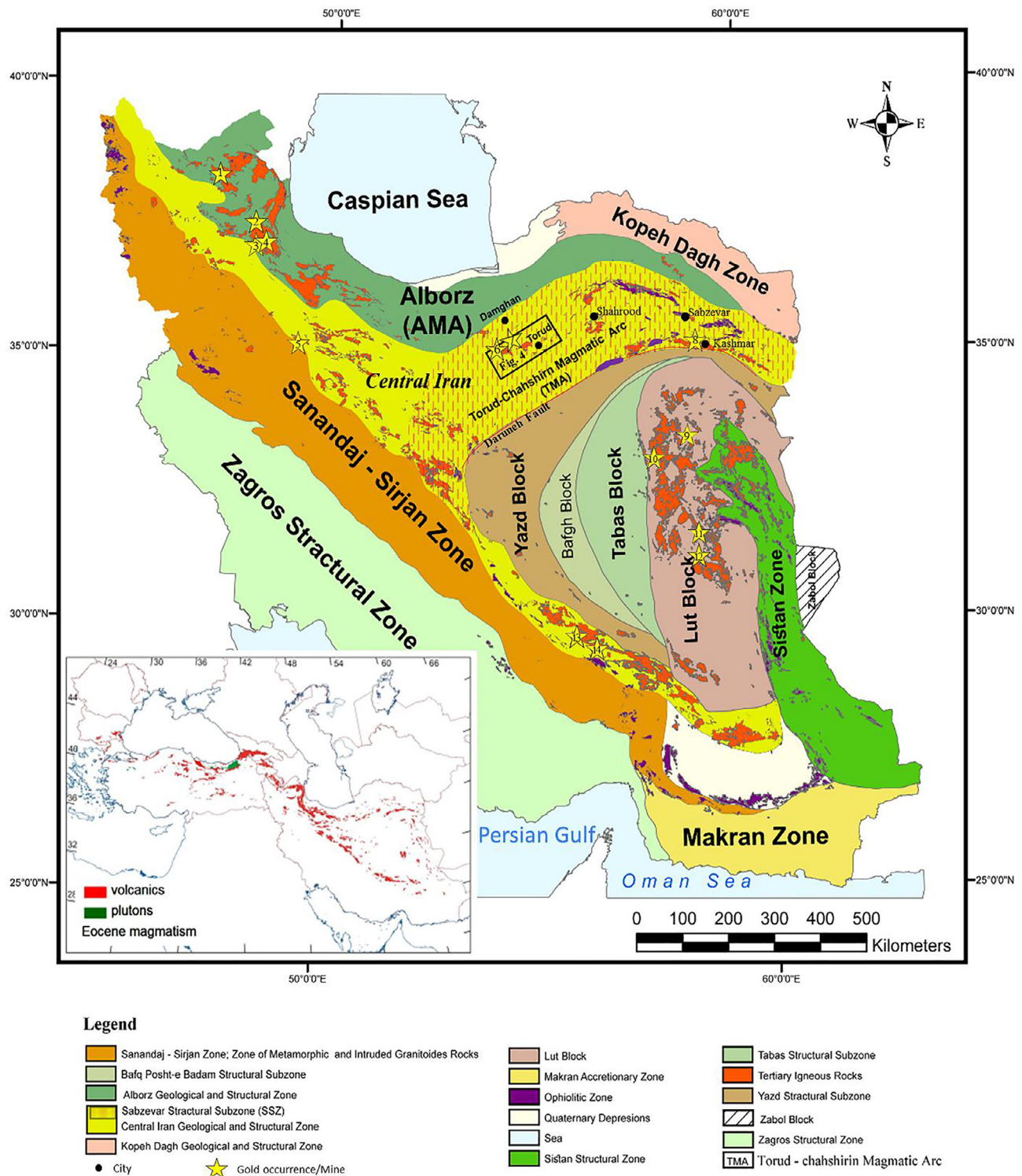


**Fig. 1.** Map showing context of Torud – Chahshirin magmatic arc (rectangle yellow dashes) within the Eocene magmatic rocks in Iranian – Turkish Plateau (inset) and first-order tectonic elements of the Iranian Plateau (modified and simplified after Stocklin, 1968; Alavi, 1991; Sahandi and Sohili, 2014). The TMA is shown with rectangle shape and location of some gold occurrences, prospects, and mines in this Cenozoic magmatic rocks: 1 = Kharvana, 2 = Mianeh, 3 = Agh Dareh, 4 = Zarshuran, 5 = Sari Gunay, 6 = Gandy-Abolhassani, 7 = Baghu, 8 = Arghash, 9 = Hired, 10 = Shadan, 11 = Qaleh Zari, 12 = Shalir, 13 = Sarcheshmeh, 14 = Chahar Gonbad (all locations are from Lescuyer et al., 2003; Shamanian et al., 2004; Moritz et al., 2006 and Richards et al., 2012, except location 8 from Ashrafpour et al., 2012). (For interpretation of the references to color in this figure legend, the reader is referred to the web version of this article.)

type; reduced) series and noted that each series had a specific metallogenic association. Characteristically, magnetite-series granitoids, or magmas with a high-oxidizing potential, form magnetite-bearing plutons that generate sulfide-rich Cu, Au, Mo, Pb, and (or) Zn deposits,

while those with low-oxidizing potential are ilmenite-series and typically generate deposits rich in tungsten and tin (Thompson et al., 1999).

Most known precious and base metals-rich deposits and occurrences in Iran are typically associated with subduction-related calc-alkaline



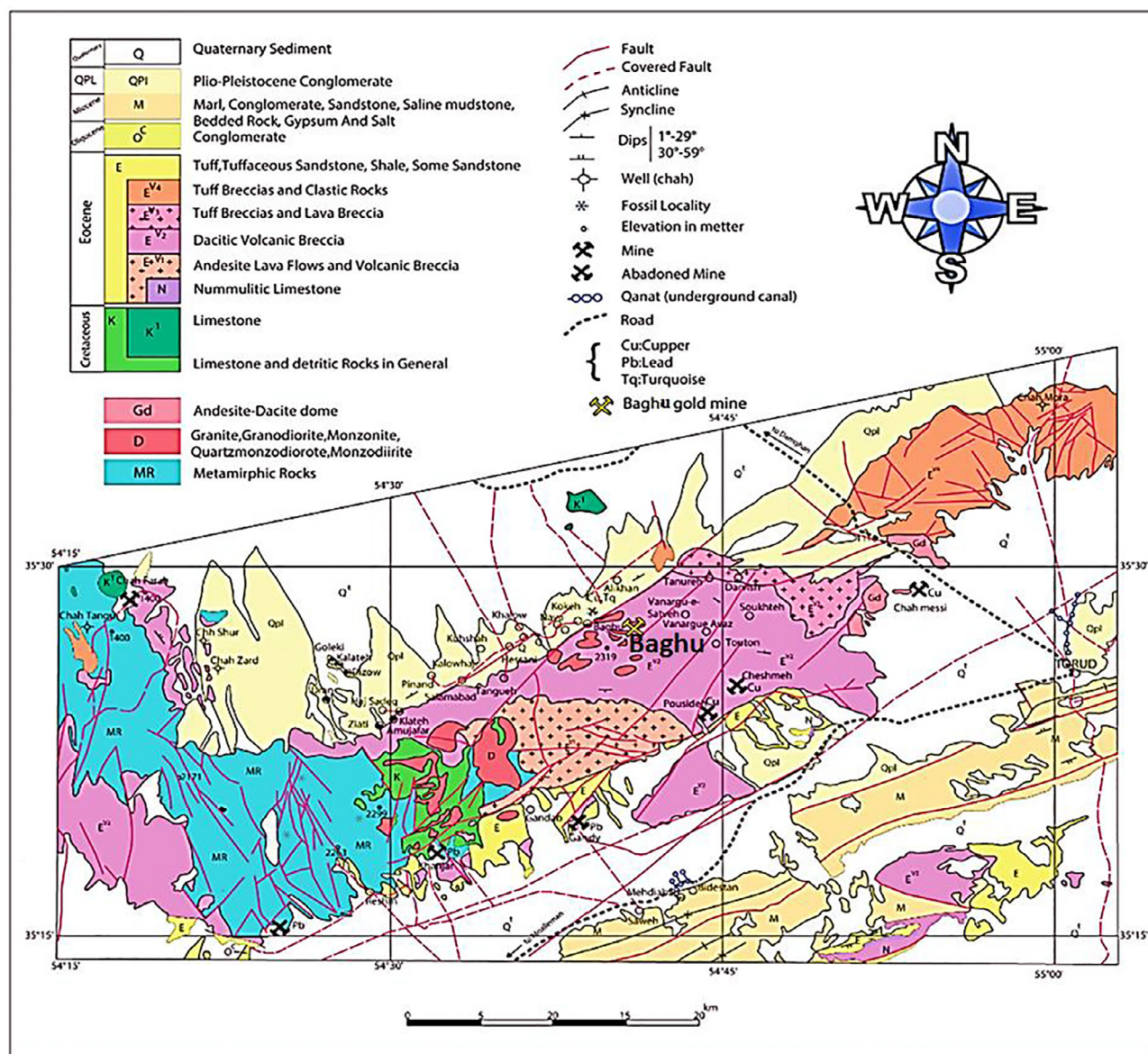


Fig. 2. Geological map of the TMA with location of mine and occurrences (modified after Houshmandzadeh et al., 1978).

Cenozoic magmatic rocks, such as at Kharvana, Mianeh, Agh Dareh, Zarshuran, Sari Gunay, Gandy-Abolhassani, Baghu, Arghash, Hired, Shadan, Qale Zari, Shalir, Sarcheshmeh, and Chahar Gonbad, (Fig. 1). Cenozoic magmatic rocks in Iran are situated around the peri-Arabian region, which is to the north of the Zagros–Bitlis suture zone. Timing of the magmatism covers the entire Cenozoic; however, gaps in the Eocene, Miocene, and Pliocene-Quaternary are conspicuous (Verdel et al., 2011; Asiabanha et al., 2012).

The most important volcanic provinces of Iran are in central Iran. The Torud-Chahshirin Tectono-Magmatic Arc (TMA) consists of Eocene volcano-plutonic complexes, which is located near the northern border of the Central Iran Magmatic Zone in Semnan province (Figs. 1 and 2). The oldest unit in this area consists of metamorphosed Precambrian basement that is overlain by Paleozoic-Mesozoic metamorphic and sedimentary rocks and Tertiary volcanic-plutonic rocks (Houshmandzadeh et al., 1978; Rahmati-Ilkhchi et al., 2010). The TMA hosts many vein-type mineral occurrences, some previously mined, that include Baghu (Au), Darestan (Au-Cu), Gandy (Au-Ag-Pb-Zn), Abolhassani (Pb-Zn-Ag-Au), Cheshmeh Hafez (Pb-Zn), Chalu (Cu), Chah-messi (Cu), Pousideh (Cu), Pb-Zn, Reshm (Pb-Zn), Khanjar (Pb-Zn), and Anaru (Pb-Zn) (Fig. 2). The gold-bearing occurrences in the TMA can be

classified as intrusion-related and epithermal, with the former also commonly containing anomalous copper concentrations. The Baghu Au ( $\pm$  Cu) deposit is an example of an oxidized intrusion-related gold system (Moradi, 2010; Shaykhi, 2013) and is the subject of this study.

The Baghu deposit is located at the site of an abandoned historic gold mine within the northern part of the TMA. It is located at  $35^{\circ}27'32.53''\text{N}$  and  $54^{\circ}39'40.43''\text{E}$  in Semnan province,  $\sim 400$  km east of Tehran and 100 km south of Damghan city in the Moaleman area. Gold- and copper-bearing veins and associated gold placers have been mined since ancient times at the Baghu deposit (Helmhacker, 1898; Henncke, 1899; Houshmandzadeh et al., 1978; Rashidnejad Omran, 1992; Tajeddin, 1999; Fard et al., 2006). The present resource estimate for the Baghu deposit is approximately 3.5 million tonnes averaging 1.17 g/t Au (IMIDRO, 2005). Our investigations are focused on the geological, structural, and geochemical controls of this intrusion-related gold mineralization in the Moaleman area. Although no world-class intrusion-related gold deposits are recognized in Iran, the potential for such deposits exists within the TMA, and thus descriptions of this historic gold system in the area should be of interest to many exploration geologists.

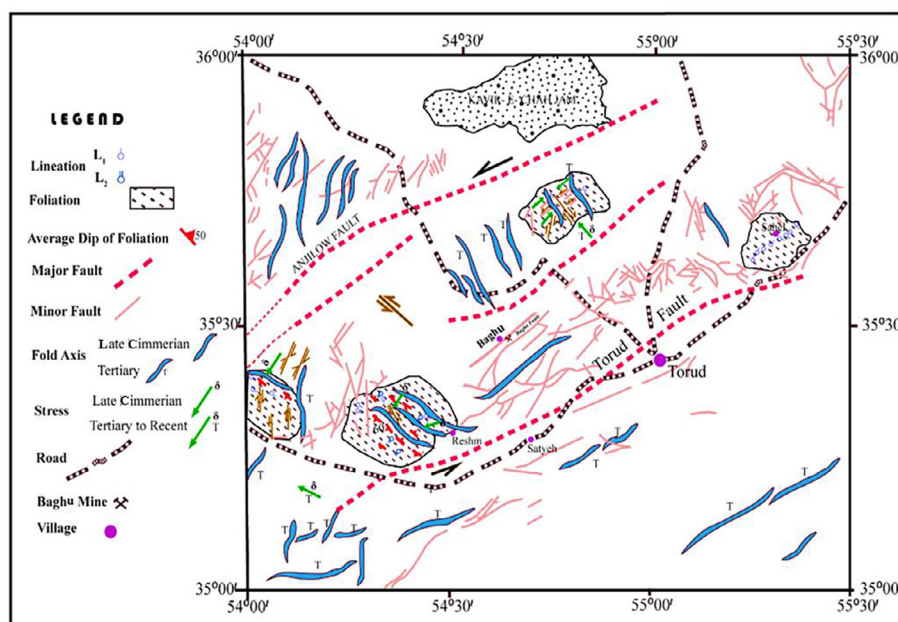


Fig. 3. TMA faults and Fractures by Houshmandzadeh et al. (1978), Ministry of Mines and Metals, Geological Survey of Iran, Scale 1: 2,500,000 with minor modified.

## 2. Geological setting

Iran is a part of the Alpine-Himalayan orogenic belt (Dercourt et al., 1986, 1993; Stampfli and Borel, 2002; Agard et al., 2005; Ghasemi and Talbot, 2006; Omrani, 2008). Three major structural units can be distinguished in Iran (e.g., Berberian and King, 1981) that include the Zagros fold-and-thrust belt (southern unit), Cimmerian blocks (central unit), and Kopet Dag Mountains (northeastern unit) (Fig. 1). The Cimmerian blocks or terranes in Iran consist of individual crustal segments that are represented by the Alborz zone, Sanandaj-Sirjan zone, and Central Iranian domain (Stöcklin, 1968; Rahmati-Ilkhchi et al., 2010). The Central Iranian domain includes the Central-East-Iranian Microcontinent (CEIM; Takin, 1972), which was surrounded by short-lived branches of the Neotethys Ocean that closed during the Late Cretaceous. Closure of the ocean basin between the northern part of the CEIM and the southern part of the Alborz Mountains is represented by the Sabzevar ophiolite (Shojaat et al., 2002) and is suggested to have led to the calc-alkaline magmatism of the TMA (Rossetti et al., 2010). Based on the work of Alavi (1991), the TMA is a part of Sabzevar Structural Zone that extends from Torbat – Kashmar – Sabzevar in the northeast to the Torud area in the southwest (Fig. 1). The TMA is bordered to the north and south by the two major faults, the Anjillo and Torud faults, respectively (Figs. 2 and 3).

The Torud-Chahshirin complex is 10–12 km wide and 100–110 km long, strikes NE–SW from Torud to Chahshirin, and parallels the Torud, Anjillo (Figs. 2 and 3), and Daruneh regional fault zones (Fig. 1). It is continuous towards the northeast and there joins the Sabzevar – Quchan – Kashmar magmatic arc (Ghasemi et al., 2014). The volcanic rocks in the complex are mainly calc-alkaline in composition and show potassium enrichment (Rashidnejad Omran, 1992; Tajeddin, 1999; Shaykhi, 2013).

The TMA Tertiary igneous rocks have a basement of metamorphosed Precambrian rocks covered by Paleozoic epicontinental sedimentary strata. Peak magmatic activity occurred in middle to late Eocene and has been divided into three stages, from oldest to youngest (Fig. 4A) as follows: (1) rhyolitic to rhyodacitic tuffs and locally andesite flows, with subordinate marls, tuffaceous marlstones, and sandstones; (2) andesite, trachyandesite, and basaltic andesite as lava flows and pyroclastic deposits; and (3) subordinate dacite-rhyodacite and hypabyssal intrusive rocks (Houshmandzadeh et al., 1978). Structural

patterns are controlled by two northeast-trending strike-slip faults, Anjillo in the north and Torud in the south (Fig. 3).

## 3. Sampling and analytical methods

About 70 selected samples were taken from several outcrops from the ore-bearing hypabyssal plutons, volcanic rocks, dikes, and altered wallrocks. Sample suites were chosen for mineralogical and petrographical studies and for geochemical analyses. Whole rock trace element concentrations were analyzed by inductively coupled plasma-mass spectrometry (ICP-MS) in China (Table 1). These analyses were carried out after sample digestion using an HF–HNO<sub>3</sub> mixture in high-pressure Teflon bombs. Pure Rh solution was used as an internal standard to monitor the drift, and reference materials were Chinese national rock standards (BHVO-2, AGV-2, G2, G3 and GSR-3). Details of analytical procedures can be found in Qi et al. (2000). The precision and accuracy of the ICP-MS analyses are estimated to be better than approximately 5% for most trace elements.

Hydrothermally altered samples were analyzed by X-ray diffraction techniques at the Geological Survey of Iran. Fourteen selected samples from quartz veins in outcrops were used for microthermometric study conducted at the Iranian Mineral Processing Research Center. Doubly polished wafers were prepared using the procedure of Shepherd et al. (1985). The thickness of the wafers varied between 80 and 200 μm, depending upon the transparency of the quartz crystals. Microthermometric studies were performed on a Linkam THMS600 heating-freezing stage. Stage calibration was performed at –56.6 °C (freezing point of pure CO<sub>2</sub>), 0.0 °C (freezing point of water), and 374.15 °C (critical point of pure water) using synthetic fluid inclusion standards (Sterner and Bodnar, 1984). Precision and accuracy were ± 0.1 °C between –70 °C and 40 °C, ± 2 °C below –70 °C, and ± 1 °C above 100 °C.

To establish the age of the host rocks for the Baghu gold deposit, three samples were selected from the andesitic subvolcanic intrusions for zircon U–Pb geochronology. Zircon separates were obtained from 6 to 7 kg of crushed rock samples by handpicking under a binocular microscope after sieving, and then applying conventional heavy liquid and magnetic separation techniques at the Geological Survey of Iran. The zircon U–Pb ages are based on U, Pb, and Th isotopic measurements employing spot analyses using the Cameca IMS 1270 ion microprobe at the University of California, Los Angeles. Analytical methods follow the



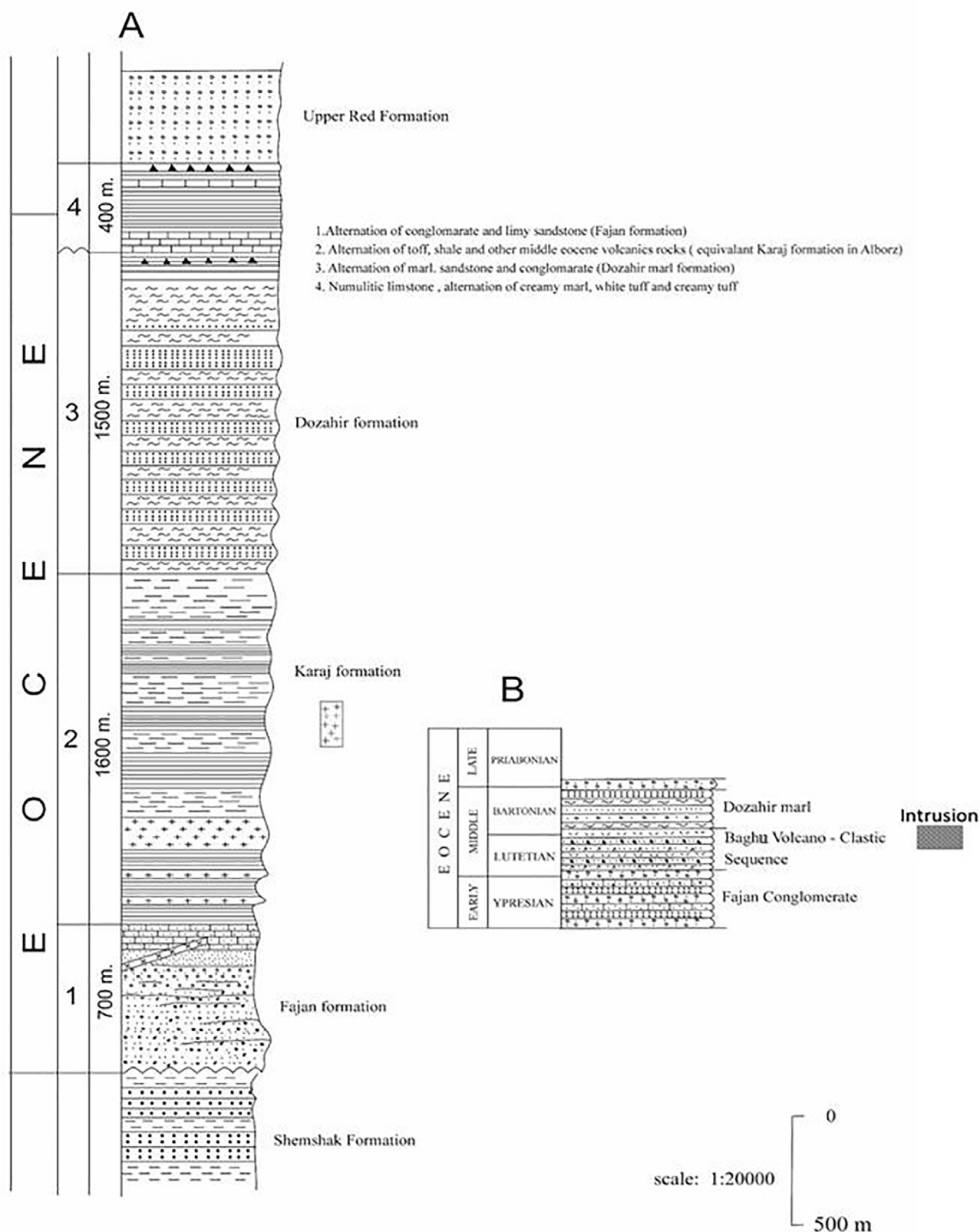


Fig. 4. (A) Eocene – Oligocene volcano – sedimentary sequence in Torud-ChahShirin mountain range with intrusive magmatism events (modified from Houshmandzadeh et al., 1978); (B) Baghu volcano-pyroclastic sequence (Rashidnejad Omran, 1992).

procedures described by Quidelleur et al. (1997) and Schmitt et al. (2003a, b). Following mineral separation using conventional heavy liquids and magnetic techniques, zircon grains were hand-selected, mounted in epoxy, and coated with  $\sim 100 \text{ \AA}$  of gold. The ion-

microprobe spot analyses utilized a primary ion beam focused to a  $\sim 30 \text{ \mu m}$  diameter spot and a secondary ion beam with a mass resolving power of 5000 and energy window of 50 eV. Following a pre-sputtering period of  $\sim 180 \text{ s}$ , each analysis collected data for 8–10 cycles. The

**Table 1**  
Whole rock major and trace element concentrations (ppm) of the Baghu deposit.

Sample Number	91-B31	91-B32	91-B33	91-B34	91-B35	91-B37	91-B38	91-B39	91-B40	91-B42	91-B45	91-B46	91-B47	91-B48	91-B49	91-B50	91-B51	91-B52	91-B53
K	21809.25	55782.64	33860.43	43364.18	32465.53	16761.68	23380.85	21364.86	30407.13	23253.61	34585.10	30129.00	27473.00	23987.00	16766.00	20003.00	28801.00	23904.00	25730.00
Ti	5280.00	1440.00	2280.00	3120.00	2400.00	5400.00	4260.00	3480.00	2280.00	2600.00	1560.00	3060.00	3060.00	2940.00	2940.00	3960.00	4200.00	5280.00	5340.00
P	6981	5073	4762	3930	3821	3914	4211	3433	2925	2015	2344	2096	1951	2240	2031	2326	4358	4267	3923
Ca	265	3.03	1.9	2.6	3.821	2.4	2.65	1.99	2.6	1.85	3.32	2.096	1.95	2.03	1.61	2.67	1.32	1.79	1.49
Rb	70.88	64.05	30.08	47.4	99.16	70.77	35.13	88.01	58.14	39.03	98.02	79.03	68.94	75.82	40.47	52.08	29.83	69.2	34.2
Ba	486.57	773.6	526.23	593.66	472.57	410.76	503.56	498.91	446.89	537.41	272.23	486	397	411	269	291	510	550	540
Th	4.27	4.2	3.03	4.69	3.93	2.13	3.24	4.2	4.01	4.85	3.86	2.98	2	2.69	1.26	2.54	7.61	8.31	8.65
U	5.21	3.35	3.77	4.73	3.98	4.75	4.12	3.75	4.18	7.18	5.21	1.01	0.86	1.18	0.6	0.91	1.78	2.04	1.73
Nb	9.69	5.07	8.35	3.52	8.89	9.69	5.13	6.27	3.36	5.72	5.21	3.36	3.13	4.34	3.49	3.44	8.41	7.57	8.75
Ta	0.84	0.39	0.45	0.48	0.49	0.51	0.47	0.47	0.25	0.28	0.22	0.21	0.23	0.21	0.22	0.24	0.52	0.49	0.51
Pb	100	66.34	50.21	39.48	79.01	119.74	27.13	79.9	110.9	30.8	93.69	77.51	32.66	41.88	57.96	30.48	12.72	13.59	12.95
Sr	815.73	306.63	380.66	438.39	300.38	820.94	712.42	680.76	333.53	958.3	615.82	540.7	571.5	915.5	865.7	837	441	696	566
Zr	43.07	39.61	29.93	36.01	16.85	40.86	51.02	51.65	28.75	66.21	30.46	34.23	41.55	35.07	59.35	34.11	85.95	99.6	89.54
Y	18.07	4.53	11.1	12.55	8.55	17.23	13.34	13.57	11.32	28.73	5.2	12.13	11.91	13.19	11.27	15.1	21.99	21.27	21.72
La	34.2	28.7	22.16	31.22	28.7	24.3	15.6	21.45	10.9	11.02	11.49	12.3	11.15	12.94	14.48	13.06	34.2	32.11	41.03
Ce	34.5	36.2	44.1	39.8	28.6	31.2	25.4	33.2	21.12	20.46	22.25	21.1	26.61	24.14	26.4	20.16	31.82	32.57	43.2
Pr	5.12	5.41	7.66	7.49	7.92	6.68	8.47	6.08	7.56	8.89	4.34	3.35	3.19	3.45	2.97	4.33	6.34	6.69	6.46
Nd	21.01	17.7	17.01	13.78	13.95	20.13	22.66	16.97	10.96	23.41	14.54	14.6–1	13.92	15.9	13.02	19.06	25.55	26.5	25.62
Sm	2.62	3.89	4.27	5.92	2.99	7.14	4.61	7.91	4.42	7.13	2.99	3.17	2.98	3.3	2.61	3.98	5.07	5.38	5.63
Eu	0.71	0.81	1.26	0.93	1.15	0.77	0.85	0.81	1.44	0.57	0.43	0.99	0.95	1.04	0.86	1.19	1.48	1.52	1.42
Gd	4.9	2.53	2.39	2.41	2.79	2.95	3.59	3.96	2.61	4.17	3.7	2.37	2.31	2.57	2.18	2.97	4.31	4.42	4.24
Tb	2.55	0.87	1.17	1.86	1.18	2.32	1.65	1.81	1.37	1.75	0.94	1.29	1.25	1.45	1.3	1.57	2.28	2.24	2.26
Lu	0.4	0.34	0.37	0.43	0.39	0.3	0.15	0.32	0.38	0.27	0.27	0.2	0.29	0.22	0.2	0.24	0.26	0.24	0.35

sample chamber was flooded with oxygen at  $\sim 3 \times 10^{-5}$  Torr to enhance secondary Pb<sup>+</sup> ionization. The reported weighted-mean ages are based on  $^{206}\text{Pb}/^{238}\text{U}$  ages calculated using zircon standard AS3 ( $1099 \pm 0.5$  Ma; [Paces and Miller, 1993](#)). Common lead corrections were made using the measured values of  $^{204}\text{Pb}$  ([Stacey and Kramers, 1975](#)) and the values of  $^{208}\text{Pb}$  corrected for  $^{232}\text{Th}$  derived  $^{208}\text{Pb}$  ([Compston et al., 1984](#)), which are considered a proxy for common  $^{206}\text{Pb}$  and  $^{207}\text{Pb}$ . These corrections use the anthropogenic Pb compositions reported for the Los Angeles basin ([Sanudo-Wilhelmy and Flégal, 1994](#)).

The Ar–Ar isotope analyses of hydrothermal white mica (sericite) were done by the stepped heating technique at the USGS laboratories in Denver, USA to date the hydrothermal gold mineralization. The mineral separates were cleaned, weighed, wrapped in aluminum foil, and encapsulated in quartz vials together with the neutron fluence monitor Hb3gr ( $t = 1073.6 \pm 5.3$  Ma, [Jourdan et al., 2006](#)). Nuclear irradiation was carried out in position B2W of the SAFARI-1 reactor, using a fast neutron flux of  $\sim 2 \times 10^{18} \text{ n cm}^{-2}$ . The J value determined from Hb3gr was  $0.01010135 \pm 0.000027$  (2 $\sigma$ ). The irradiated samples were step-heated in a Ta-resistance furnace from 500 to 1600 °C, using 30 min heating steps. During heating, Ar was purified using a Zr–Al getter at 450 °C and transferred to an MS1 mass spectrometer for isotope measurements. The data obtained were corrected for mass discrimination (calibrated using atmospheric argon), radioactive decay, and neutron interference corrections. See [Burgess et al. \(2004\)](#) for further experimental details. The Ar–Ar ages were determined from an age spectrum diagram, using the ISOPLOT/Ex 3.23 software ([Ludwig, 2003](#)). All ages are reported at the 2 $\sigma$  level of uncertainty.

Oxygen and sulfur isotope analyses were completed at the USGS laboratories in Denver. A CO<sub>2</sub> laser fluorination method was used to analyze oxygen isotopes at USGS laboratories, along with a Finnegan Delta Plus mass spectrometer in continuous-flow mode. The external precision and accuracy per sample is  $\pm 0.2$  per mil. The sulfur isotope analyses were measured via EA-IRMS also using a Finnegan Delta Plus mass spectrometer. Reproducibility, as determined from replicate measurement, was better than 0.2 per mil.

#### 4. Geology of the Baghu deposit

The Baghu gold deposit, with mineralized rocks exposed over an area of about 40 km<sup>2</sup>, has been mapped in this study ([Fig. 5](#)). The most significant hypogene alteration and ore zones are concentrated in a 1.2 km<sup>2</sup> area. This area is a part of a NE-trending horst within the TMA. The rocks in the vicinity of the Baghu deposit consist of Eocene intermediate to acidic lava flows of andesite, trachyandesite, and dacite; volcanic breccias; epizonal subvolcanic intrusions, which include diorite, granodiorite, and micro-granite; and several dikes ([Figs. 4B and 5](#)). The host rocks for the gold deposit are the granodiorite and micro-granite.

The chondrite-normalized ([Boynnton, 1984](#)) rare earth element (REEs) abundance pattern of the Baghu igneous rock samples exhibit an enrichment of light rare earth elements (La, Ce, Pr, Nd, and Sm) relative to heavy rare earth elements (Dy, Yb, Lu) and Y ([Fig. 7A; Table 1](#)). A primitive mantle-normalized spider diagram patterns ([Sun and McDonough 1989](#)) of the Baghu samples ([Fig. 7B; Table 1](#)) are also characterized by enrichment in large-ion lithophile elements (Rb, Ba, U, and Pb) and depletion in high-field strength elements (Nb, Zr, and Ti). The distinct negative Nb and Ti anomalies of the Baghu samples also suggest that their source region may have melted under high pressure conditions in which garnet was a residual phase at a pressure of more than 1.5 GPa (e.g., [Xiong et al., 2006; Asadi, 2013](#)). Such evidence implies that the crust beneath the region was thickened during the Tertiary, which is typical of arc igneous rocks (e.g., [Pearce and Peate, 1995](#)).

The stratigraphy of the igneous rocks at Baghu ([Fig. 4B](#)) has a lowest sequence of thin-bedded green to purple trachydacite and dacite tuffs, and massive gray dacite to dacitic andesite tuff breccia. These are



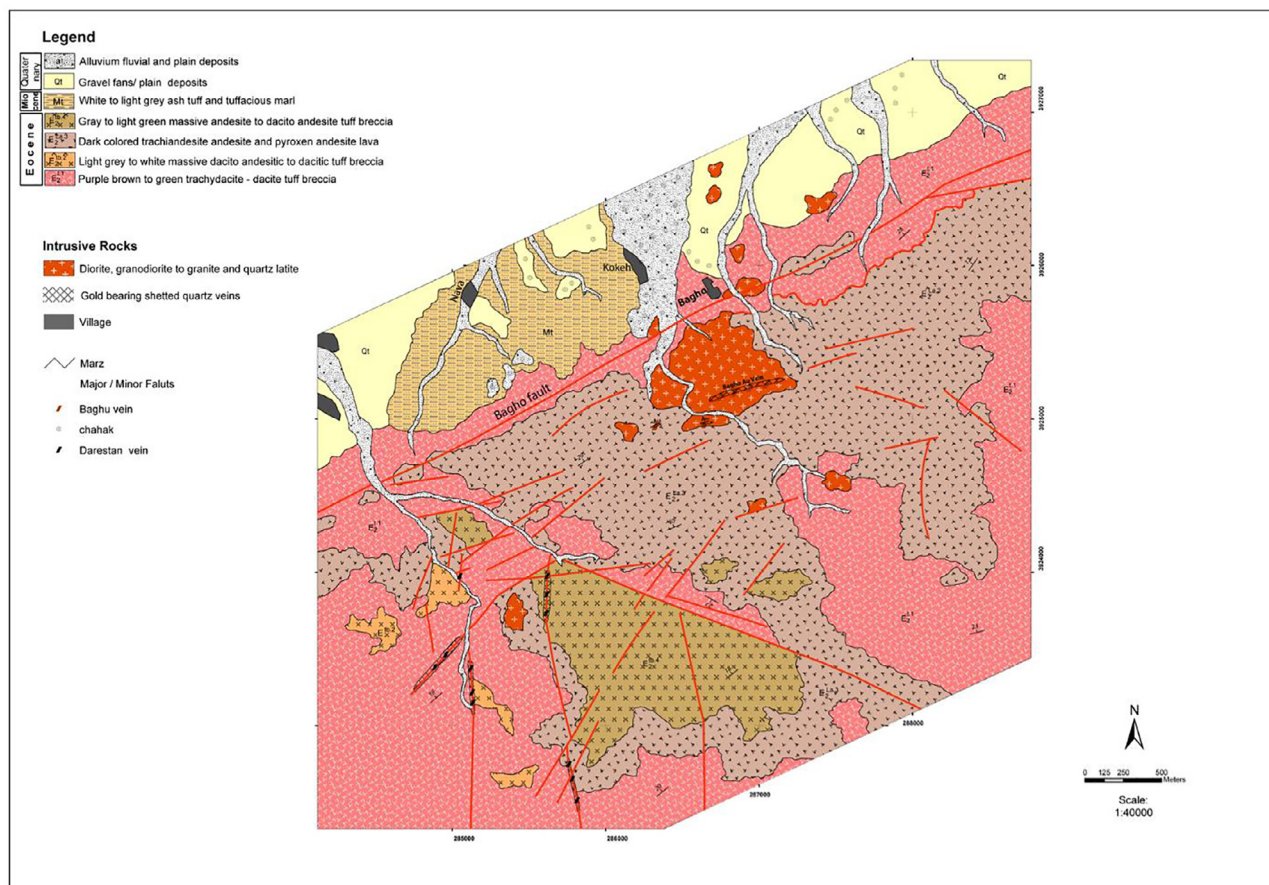


Fig. 5. Geological map of Baghu deposit (modified after Tajeddin, 1999).

overlain by andesite and trachyandesite flows, and then an andesitic to dacite andesitic unit comprising gray to green tuffs, volcanic breccias, and intermediate lava flows. Zircon U–Pb SIMS dating of this latter unit yields an age of  $ca. 47.5 \pm 2.4$  Ma (Fig. 8A). Subvolcanic cryptodomes, hypabyssal plutons, and several dikes intrude the volcanic sequence. Zircon U–Pb SIMS dating of a number of these igneous bodies yielded an age of  $ca. 43.4 \pm 1.3$  Ma (Fig. 8B). In addition, zircon U–Pb SIMS dating of a basic dike near the deposit yielded an age of  $38.0 \pm 0.9$  Ma (Fig. 8C and Table 2).

The igneous rock units in the Baghu area are located between the Torud fault in the south and Anjillo fault in the north. The units in the area of the deposit are highly fractured within a broad zone of shearing (Fig. 3) and this deformation zone served as the conduit for the hydrothermal fluid. However, pure tensional fractures are not the only structural control on the gold-bearing veins. Open space for mineral deposition seems to also have been controlled by Riedel (R) and anti-Riedel (R') conjugate shear fractures (e.g., Riedel, 1929; Moore, 1979; Davis et al., 1999; Ahlgren, 2001; Katz et al., 2004).

The TMA contains many fracture and faults that formed during left-lateral shear motion. Dikes and related fractures show tensional features in the western and central parts of the TMA as confirmed by the T-, R-, and D-type fractures. These R-, R', and D-type fractures also localized the mineralized veins (Keynezhad et al., 2010). In the mapped area, the Baghu fault is accompanied by minor faults and joints that conform to the D-type of left-lateral shearing (Fig. 9). The fractures and faults in the mapped area have been divided into four different groups that trend NE–SW, NW–SE, N–S, and E–W. Those with 40–70° E strikes and 60–70° SE dips were formed by movement on the NE-trending Torud fault. Dikes in the Baghu deposit that are NW-trending are related to R-type fractures, but some that show an E–W trend are associated with P-type fractures (Fig. 10).

## 5. Mineralization and hydrothermal alteration

Hydrothermal alteration and mineralization at the Baghu gold deposit are centered on the hypabyssal granodiorites and microgranite (Fig. 11A). The mineralization is structurally controlled by extensional brittle faults and fractures, present as sheeted quartz veins sub-parallel to the Anjillo and Baghu faults (Fig. 11B). A major quartz-tourmaline vein occupies a normal dip-slip fault (Fig. 12A). This main vein averages 10–70 cm in thickness and extends for ~1 km with a NE–SW strike. Extensional veins, which trend N60E and dip 60–75°, are also locally gold-rich (Fig. 10). Principal metallic minerals in the veins include native gold, pyrite, pyrrhotite, chalcopyrite, bornite, sphalerite, magnetite, covellite, digenite, chalcocite, malachite, and Fe-hydroxide. Anhedral to euhedral native gold ranges in size from 10 to 300  $\mu$ m. Open-space filling and brecciation are common (Figs. 11C, 12B and C, 14, 15). The Au grade in the main vein locally reaches 57 g/t, but averages 2.6 g/t. The Au grade in sheeted quartz veins that are parallel to the main quartz – tourmaline vein is also significant and is locally as high as 0.8 g/t (Babakhani et al., 1996; Rastad et al., 1999).

Cross-cutting vein systems define a two-stage paragenetic sequence (Fig. 12B and C). Stage I is identified by fine-grained quartz, less than 0.2 mm in diameter, associated with minor pyrite, chalcopyrite, and tourmaline. The grade of gold in this early stage averages only 0.25 g/t. These pre-ore veins are located in the central parts of the subvolcanic intrusions and show minor potassic alteration characterized by adularia. Structural irregularities suggest that the veins formed at relatively high temperatures, when the rock was relatively ductile, probably shortly after the stock consolidated. They vary in width from 1 to more than 5 cm.

Stage II veins include quartz, sericite, tourmaline (schorlite – dravite), pyrite, pyrrhotite, magnetite, chalcopyrite, bornite, sphalerite,



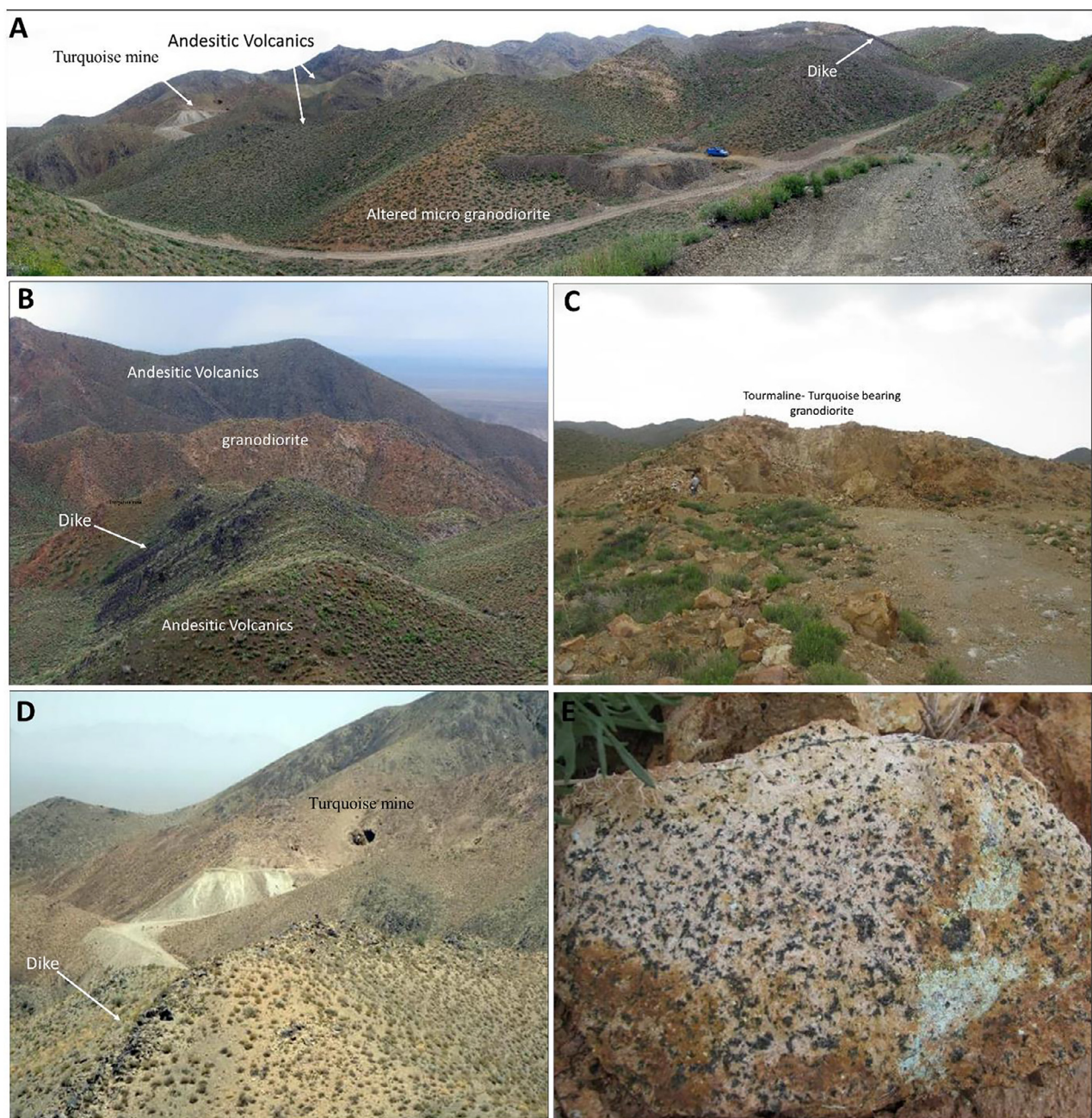


**Fig. 6.** (A) Panorama view of the main volcano-plutonic units at the Baghu gold deposit, looking SSW. Hydrothermal alteration is characterized by the supergene bleaching. Lavas exposed in the green hill and subvolcanic intrusions show with creamy to brown on the photo. On the east- upper of photo show a post-Eocene dioritic dyke that cut the Middle-Upper Eocene succession; (B) Epizonal subvolcanic intrusions (light Brown color), which include, granodiorite, and micro-granite; and several dikes; (C) granodiorite subjected B; (D) The Baghu Turquoise mine in granodioritic rocks; (E) a close up photo of subjected rocks in D. The highly altered and bleached plutonic rocks containing tourmaline, turquoise, pyrite, and quartz in the Baghu turquoise mine. (For interpretation of the references to color in this figure legend, the reader is referred to the web version of this article.)

and native gold (Fig. 13). The grade of gold mineralization in this stage averages 1.5 g/t. Gold content in the ore correlates with sulfide mineral abundance. The quartz veins that formed during this stage are coarse grained and grains are 0.5 to 1.0 mm in diameter. Dating of hydrothermal sericite from a stage II vein by  $^{40}\text{Ar}/^{39}\text{Ar}$  methods indicates a mineralization age of ca. 44 Ma (Fig. 14).

Hydrothermal tourmaline commonly occurs as disseminations, aggregates, pods, and veins within the intrusive rocks, or as alteration envelopes and veins along pluton contacts and in the Eocene volcanic country rocks associated with the widespread phyllic alteration. Petrography and electron probe microanalysis indicate that the

tourmaline belongs to the schorlite-dravite solid solution with a tendency toward schorl end-member (Ghorbani et al., 2006). The B-bearing fluids were sourced from metapelites and metapsammities co-existing with Al-saturated phases. It is probable that the tourmaline was generated from hydrothermal fluids reacting with sericite in the phyllic alteration zone (Taghipour and Mackizadeh, 2014). The peripheral propylitic alteration at the Baghu deposit is characterized by formation of montmorillonite, chlorite, epidote, calcite, quartz, and pyrite (Fig. 11).

The supergene overprint is significant at the Baghu deposit. The resulting bleaching has made the ore deposit distinctive from the dark-



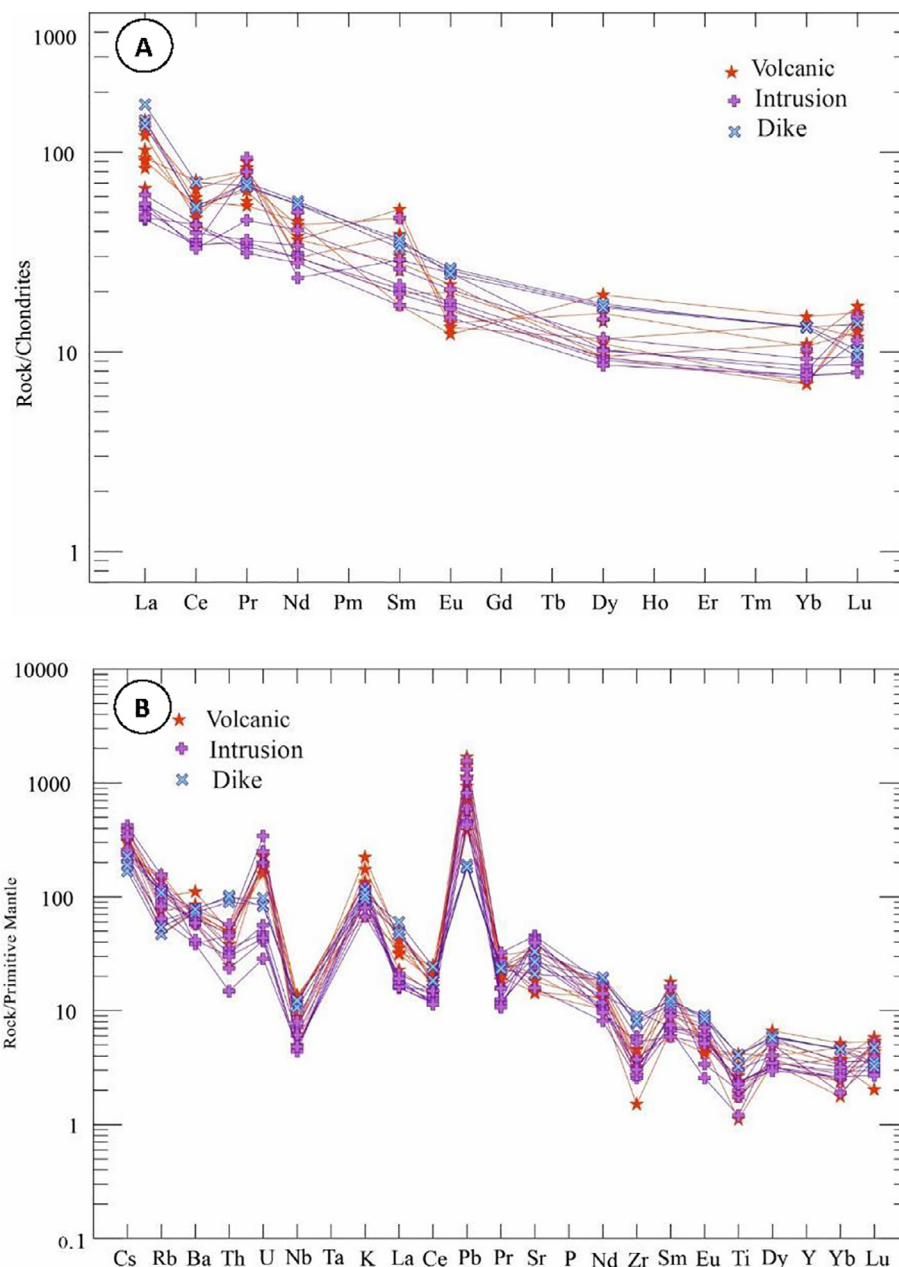


Fig. 7. (A) Chondrite-normalized (values given in Boynton, 1984) rare earth element (REE) abundance pattern samples of the Baghu gold deposit; (B) Primitive mantle-normalized multielement variation patterns (normalized to values given in Sun and McDonough, 1989) of the Baghu gold deposit rock samples.

colored volcano-sedimentary host rocks. Kaolinite and iron oxy-hydroxides are widespread. Iron oxy-hydroxides have replaced up to 50 percent of the hypogene sulfide minerals, and locally, the grade of the mineralization is as high as 57 g/t Au (Fig. 15A–H). Malachite, azurite, covellite, digenite, and chalcocite are also present.

Turquoise is conspicuous in fractures in the Baghu area, particularly in the highly altered plutonic rocks containing pyrite, quartz, and tourmaline (e.g., in the Baghu turquoise mine; Fig. 6A–E). The turquoise is associated with iron oxides (goethite-hematite) and quartz in veinlets and coatings. Also, it occurs as disseminated, small, sub-rounded nodules in sericitized to weakly kaolinitized volcanic rocks. Spatial associations and stable isotope data ( $\delta^{18}\text{O}$  and  $\delta\text{D}$ ) for turquoise indicate that it is part of the overprinting supergene mineral assemblage (Taghipour and Mackizadeh, 2014).

## 6. Fluid inclusion microthermometry

### 6.1. Samples and methods

The morphology and petrographic characteristics of fluid inclusions in ore-related quartz were recorded at room temperature using the criteria of Roedder (1984) and Shepherd et al. (1985). The inclusions were classified on the basis of host mineral occurrence, their relationship to each other, and the type of inclusions. With respect to their relationship to the host mineral, they are classified as primary (isolated inclusions, as well as those in growth zones), secondary (inclusions occurring along fractures that intersect the crystallographic surfaces), and pseudo-secondary (inclusions occurring along fractures that do not intersect the crystallographic surfaces). Pseudo-secondary and necked inclusions were avoided for study.

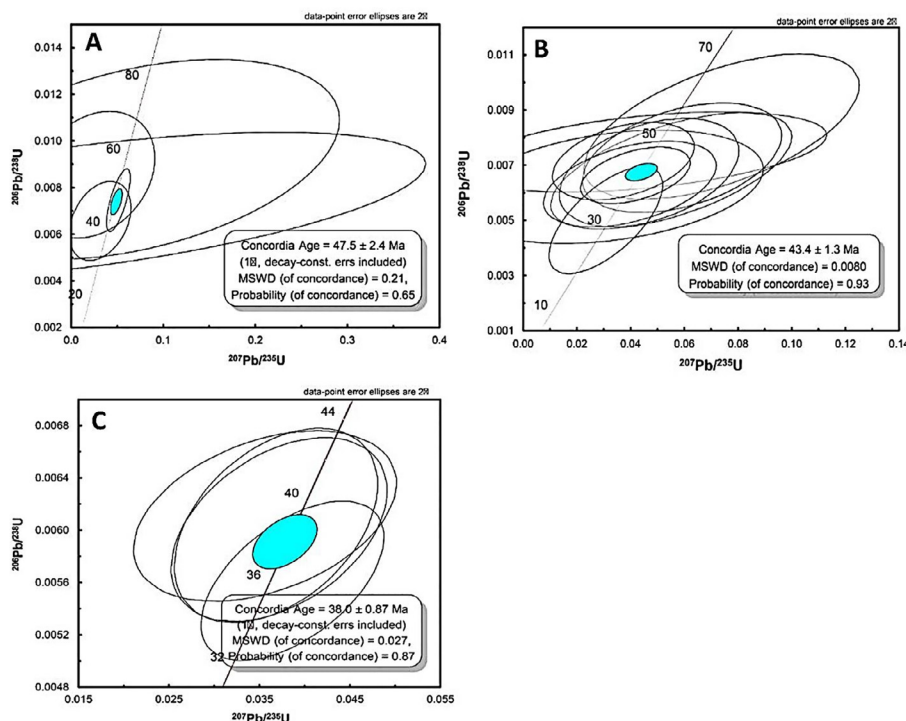


**Fig. 8.** The LA-ICP-MS zircon U-Pb concordia diagrams for the volcano-plutonic units at the Baghu gold deposit (A) subvolcanic granodiorite; (B) and (C) dioritic dyke. Circles represent analyzed spots, and numbers represent  $^{206}\text{Pb}/^{238}\text{U}$  ages.

**Table 2**

U-Pb ages for volcano- plutonic rock types of the Baghu gold deposit.

Sample ID	UTM (WGS84)	Rock type	Age (Ma)	1 sigma age error (Ma)
B41	287181.00E 3925933.00N	Microgranodiorite	43.4	1.3
TRU5	284757.77E 3924273.23N	Andesite	47.5	2.4
TRU9	287526.00E 3926151.00N	Diorite	38.0	0.87

Sample selection was biased to quartz that contained an abundance of ore-related sulfide minerals and/or high gold grades, and which was collected in the main adit and from surface outcrops. We could not study fluid inclusions smaller than about 5  $\mu\text{m}$  in maximum dimension and we avoided those that were necked. Data were mostly obtained from inclusions ranging in diameter from 10 to 100  $\mu\text{m}$ . All abbreviations and terminology of fluid inclusions are as referred to in Diamond (2003a).

## 6.2. Fluid inclusion petrography

Fluid inclusions in stage I quartz are very small and unsuitable for microthermometric measurements. All microthermometric measurements were therefore carried out on samples of stage II quartz (Fig. 16A–H). Based on the number of phases at room temperature and their microthermometric behavior, and using the criteria of Roedder (1984), Shepherd et al. (1985), and Goldstein (2003), five fluid inclusion types were recognized (Fig. 17): I. Monophase liquid liquid; II. monophase gas; III. Two-phase liquid and gas (aqueous liquid + vapor); IV. Two- or three-phase carbonic-aqueous (aqueous liquid + carbonic phase [ $\text{LCO}_2$  or  $\text{LCO}_2 + \text{VCO}_2$ ]); and V. multi-solid (liquid–vapor–solid) inclusions. The type V inclusions are divided into three subtypes based on solid phases:  $\text{V}_I$ . two-phase liquid and solid (aqueous liquid + halite),  $\text{V}_{II}$ . three-phase liquid, solid, and gas (aqueous liquid + vapor +

halite  $\pm$  sylvite), and  $\text{V}_{III}$ . multi-phase, liquid, multi-solid, and gas (aqueous liquid + vapor + halite  $\pm$  sylvite  $\pm$  mica  $\pm$  anhydrite?  $\pm$  boric acid [ $\text{H}_3\text{BO}_3$ ] + opaque minerals, such as pyrite, chalcopyrite, and hematite). Types III and V are the most abundant inclusions and account for 80 percent of the inclusion population.

Type I inclusions contain one phase liquid at room temperature (Fig. 17A). The inclusions are irregular, rounded, or rectangular in shape. The size of the inclusions varies between 10 and 50  $\mu\text{m}$ . Type II inclusions appear to contain solely a vapor phase (Fig. 17A) that optically occupies the entire volume of the inclusion, although as much as 5 vol% liquid surrounding the vapor phase could go unnoticed in such inclusions. Type II inclusions have a regular sub-rounded to rectangular shape, and a size of 10–40  $\mu\text{m}$ . Type III inclusions (Fig. 17B) can be divided in two groups, with one set of inclusions being liquid-rich (IIIA) and containing two phases at room temperature with the bubble occupying 40–50 percent of the total inclusion volume. The other set is vapor-rich (IIIB) and inclusions contain two phases at room temperature with the bubble occupying 60–90 percent of the total inclusion volume. Both groups of type III inclusions are faceted, rounded, and subrounded, with sizes generally less than 45  $\mu\text{m}$ .

Type IV inclusions have two or three phases at room temperature. The three-phase inclusions contain a vapor bubble at room temperature filling 40–70 percent of the total inclusion volume. These inclusions are faceted to subrounded and the largest has diameters up to 50  $\mu\text{m}$  (Fig. 17C). This type of inclusion occurs in gold-bearing late stage II quartz.

Sub-type  $\text{V}_I$  inclusions contain two phases at room temperature. The two-phase inclusions contain a liquid and solid at room temperature, filling 40–60 percent of the total inclusion volume. The solid phase consists of predominantly cubic halite; these inclusions are faceted to subrounded and up to 60  $\mu\text{m}$  in size (Fig. 17D). Sub-type  $\text{V}_{II}$  and  $\text{V}_{III}$  inclusions exhibit multiple phases at room temperature. The multiphase inclusions contain a liquid, solid(s), and gas, with a vapor bubble at room temperature filling 50–60 percent of the total inclusion volume. These inclusions are faceted to subrounded, have negative crystal shape, are highly saline, and up to 85  $\mu\text{m}$  in size (Fig. 17E). The



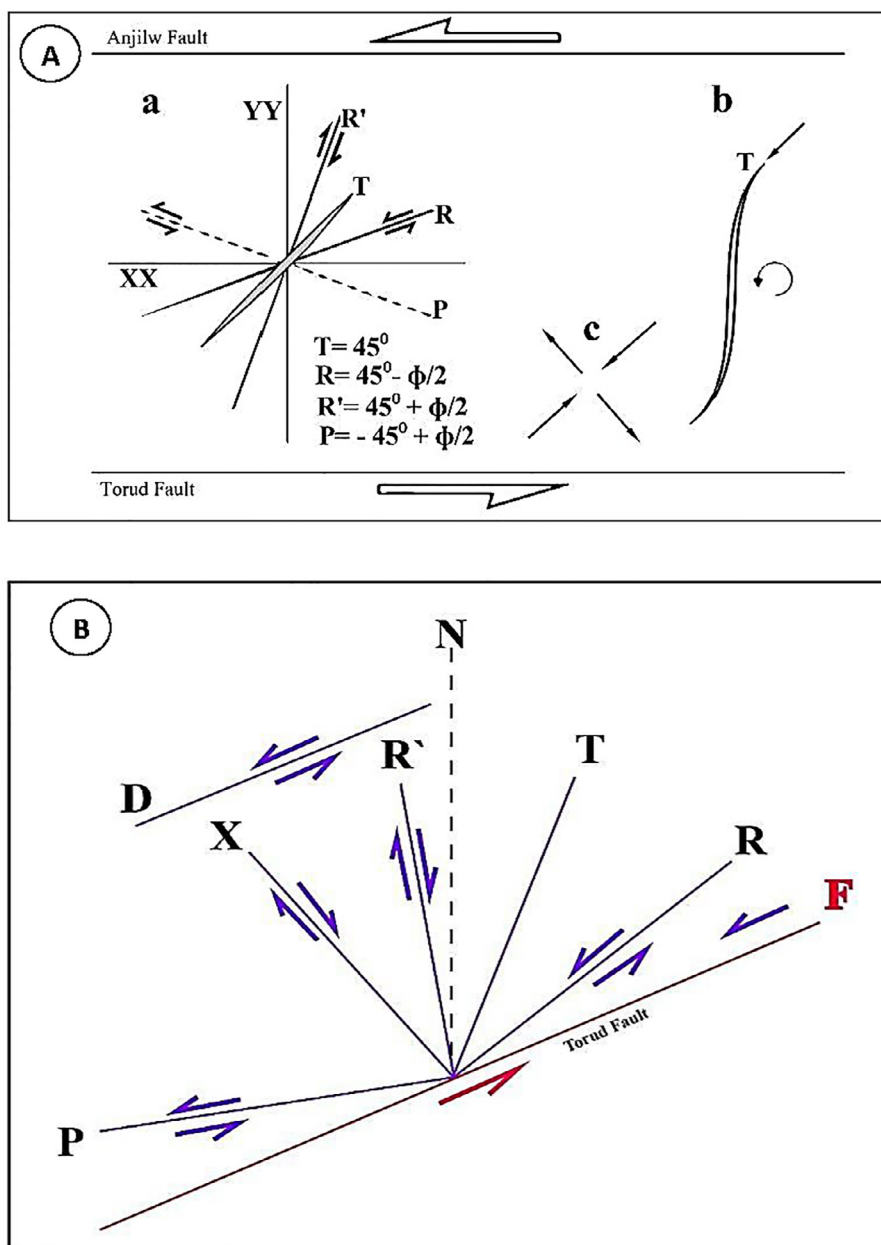


**Fig. 9.** (A) (a) Geometry of an idealized tension gash in sinistral simple shear; (b) theoretical distribution of tensional fractures (T) and shear fractures (R, R' and P) in the same kinematical framework. (c) Instantaneous stretching axes. (B) The situation of all type of fractures related to Torud fault shear zone, [Keynezhad et al. \(2010\)](#).

daughter phase is predominantly cubic halite, locally accompanied by round sylvite; also other daughter minerals, such as mica, anhydrite, and tourmaline can be distinguished. Solid phases, mainly sulfides, such as pyrite and chalcopyrite, and rarer oxides, such as hematite and unidentified opaque minerals, may constitute less than 1 percent volume of an inclusion ([Fig. 17F](#)). In these inclusions, the distribution and volume of solid phases are inconsistent, suggesting that they represent trapped solids rather than daughter minerals. The inclusions are isolated or most commonly form trails and clusters in the veins.

### 6.3. Microthermometric results

Microthermometric measurements and volume fraction estimates of the different phases were evaluated utilizing the FLUIDS ([Bakker, 1999](#)) and CLATHRATES ([Bakker, 1997](#)) programs, so to utilize melting and homogenization temperatures and optical volume fraction to estimate

bulk compositions and densities. Salinities were estimated after [Bodnar \(1993\)](#) from final ice melting ( $T_m(\text{Ice})$ ) of aqueous inclusions and after [Bakker \(1997\)](#) from clathrate melting ( $T_m(\text{Cla})$ ) for aqueous-carbonic inclusions. The salinities of multiphase-bearing fluid inclusions were calculated using the dissolution temperatures of daughter minerals ([Hall et al., 1988](#)). Densities of  $\text{H}_2\text{O}$ -,  $\text{CO}_2$ -, and  $\text{NaCl}$ -bearing fluid inclusions are calculated from the equation of state by [Zhang and Frantz \(1987\)](#), [Holloway \(1981\)](#), and [Bowers and Helgeson \(1983\)](#) for the  $\text{H}_2\text{O}$ - $\text{CO}_2$ - $\text{NaCl}$  system.

For the isochore calculations, we used the program FLINCOR ([Brown 1989](#)). In addition, for pressure estimates in two-phase aqueous inclusions, we used the equation of state for  $\text{H}_2\text{O}$  in a P–T projection ([Diamond, 2003a](#)). Also for  $\text{H}_2\text{O}$ - $\text{CO}_2$ - $\text{NaCl}$  and  $\text{H}_2\text{O}$ - $\text{NaCl}$  fluid inclusions systems, we used equations of state from [Bowers and Helgeson \(1983\)](#), and [Zhang and Frantz \(1987\)](#), in MacFlinCor computer programs ([Brown and Hagemann, 1994](#)). Microthermometric

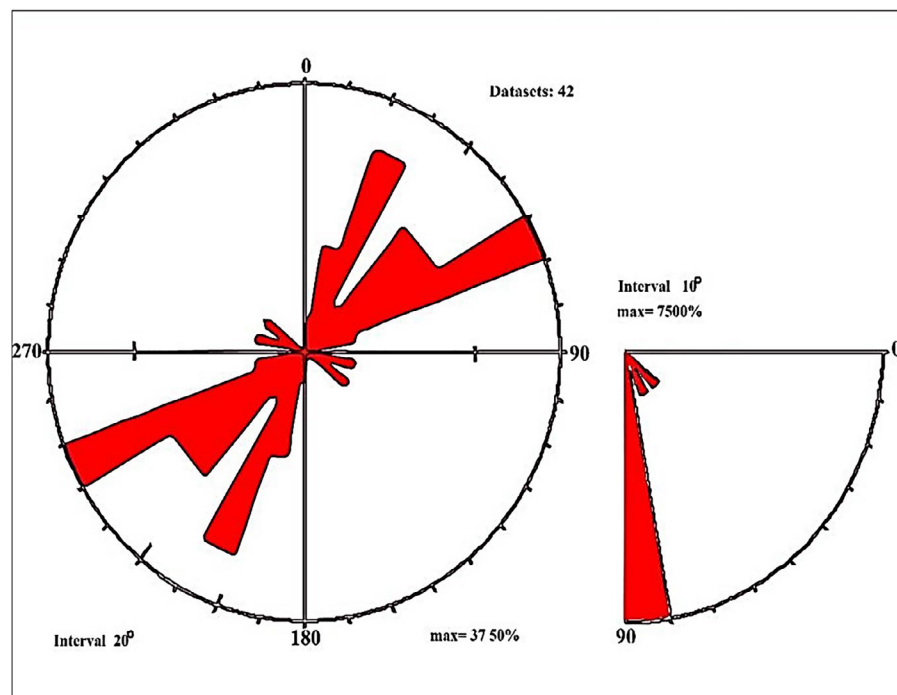


Fig. 10. Rose diagrams for the fault and fractures from the Baghu gold deposit. Inside, the situation of all type of fractures related to Torud fault shear zone.

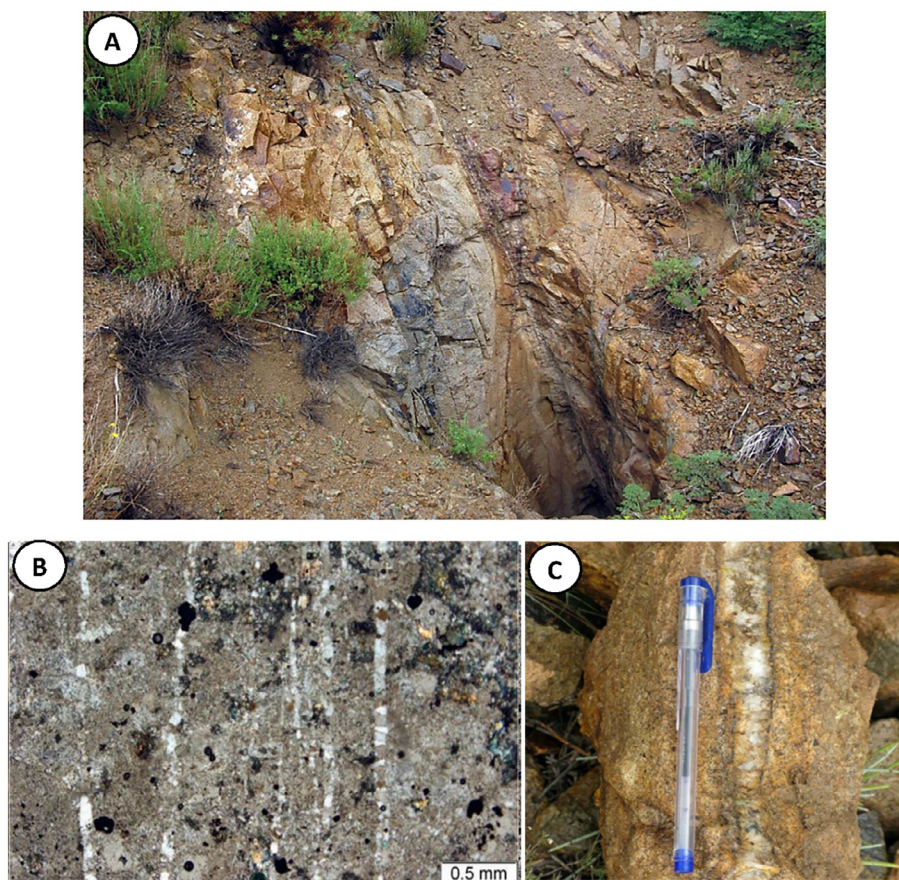
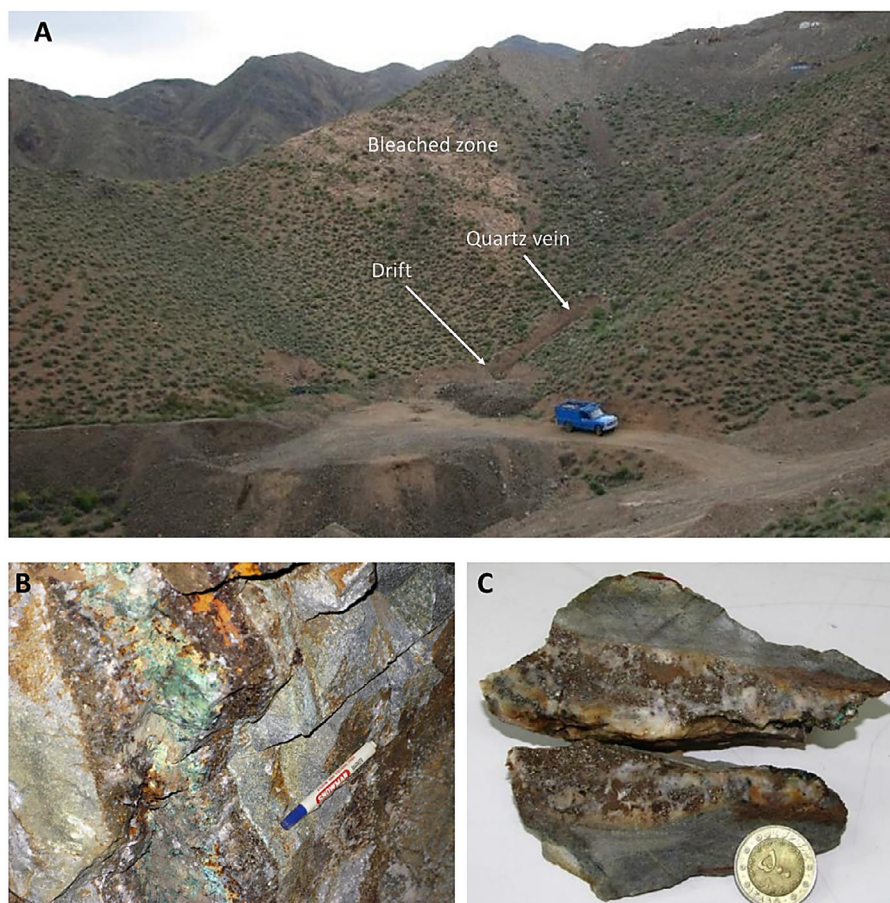


Fig. 11. Photographs of the wall-rock granodiorite from the Baghu gold deposit (A) gold bearing quartz –tourmaline sheeted vein in the granodioritic rocks; (B) Photomicrographs from micro granodiorite subjected Figs (A) and (C) A close up of the sheeted quartz -tourmaline gold vein Au-bearing sulfide ore.





**Fig. 12.** (A) Photographs of bleached micro- granodiorite hosted of mineralization and a drift in the main quartz vein gold bearing from the Baghu gold deposit. (B) and (C) the main veined Au-Cu bearing polymetallic sulfide ore; subjected Fig A.

measurements for 291 primary fluid inclusions are summarized in Table 3.

The average total homogenization temperature ( $T_h$ ), to a liquid or vapor, of type III and IV primary inclusions in quartz ranges from 180 to 382 °C, with a mode at 280 °C. The  $T_m(\text{Ice})$  of type III fluid inclusions ranges from −15.0 to −0.5 °C, indicating low to moderate salinities between 0.5 and 15.7 wt% NaCl equiv, with a mode at about 4.2 wt% NaCl equiv. The type IV aqueous-carbonic inclusions ( $\text{H}_2\text{O}-\text{CO}_2 \pm \text{CH}_4 \pm \text{N}_2$ ) showed  $\text{CO}_2$  melting ( $T_m(\text{CO}_2)$ ) ranging from −61.0 to −56.3 °C. This range continues to values significantly lower than the melting temperature of pure  $\text{CO}_2$  (triple-phase point is −56.6 °C), suggesting minor amounts of dissolved  $\text{CH}_4$  and/or  $\text{N}_2$  in addition to  $\text{CO}_2$  (Dreher et al., 2007; Volkov et al., 2011). The  $\text{CO}_2$  homogenization temperature ( $T_h(\text{CO}_2)$ ), typically to a liquid, was in the range from +23.8 to +30.4 °C. Clathrate melting was determined in the inclusions to be between +3.1 °C and +8.5 °C, indicating fluid salinities of about 3.8–11.5 wt% NaCl equiv. (Fig. 18A–H).

The final homogenization temperatures for the type  $V_I$  primary inclusions varied between 185° and 433 °C (average 300 °C), based on halite dissolution. This corresponds to high salinities of 33–45 wt% NaCl equiv. These hypersaline fluid inclusions always homogenized to liquid. Fluid inclusion types  $V_{II}$  and  $V_{III}$  contain chalcopyrite, pyrite, and other opaque minerals (accidental) that do not melt during heating runs, whereas the halite daughter phases dissolved at 198–490 °C ( $T_m$  (Halite)), corresponding to high salinities of 40–52 wt% NaCl equiv. These hypersaline fluid inclusions had final homogenizations to liquid or to vapor at temperatures of 235–590 °C, with a 355 °C modal value. Only a few inclusions were observed with a  $T_h$  above 500 °C (Fig. 18A–H).

The homogenization temperatures for the type IV aqueous-carbonic fluid inclusions were used here as an estimate of trapping temperatures; all values were above 280 °C. The trapping pressures of the fluid inclusions were estimated to be from 94 to 132 MPa, which corresponds to a depth of 2550–3883 m, assuming a pressure gradient of ~26.4 MPa per km based on MacFlinCor computer programs (Brown and Hagemann, 1994).

## 7. Stable isotope studies

Stable isotope studies were conducted to help determine ore fluid source reservoirs. The  $\delta^{18}\text{O}$  values (relative to SMOW) for eleven analyzed quartz samples, collected from several sulfide-rich stage-II veins with high gold grades, fall in a narrow range from 11.6 to 13.9 per mil, with an average of 12.6 per mil (Table 4). Assuming a quartz deposition temperature of 450 °C obtained from fluid inclusion study, calculated values using Zheng (1993) for  $\delta^{18}\text{O}$  fluid range between approximately 8.0 and 10.3 per mil with an average of 8.9 per mil. Although typically the origin of the fluid is established by coupled analysis of both O and H stable isotopes, these high and consistent  $\delta^{18}\text{O}$  fluid values can be nevertheless interpreted to suggest that the hydrothermal fluid is magmatic in origin.

Sulfur isotope ratios were determined for pyrite and chalcopyrite separated from gold-bearing veins. The eleven  $\delta^{34}\text{S}$  measurements (relative to CDT) range from +1.5 to +3.1 per mil with an average of 2.1 per mil (Table 5), which is also consistent with a reduced magmatic source of sulfur (Ohmoto and Rye, 1979; Rye, 1993; Kouzmanov and Ramboz, 2003; Moritz et al., 2003; Seal, 2006; Yilmaz et al., 2007, 2010).

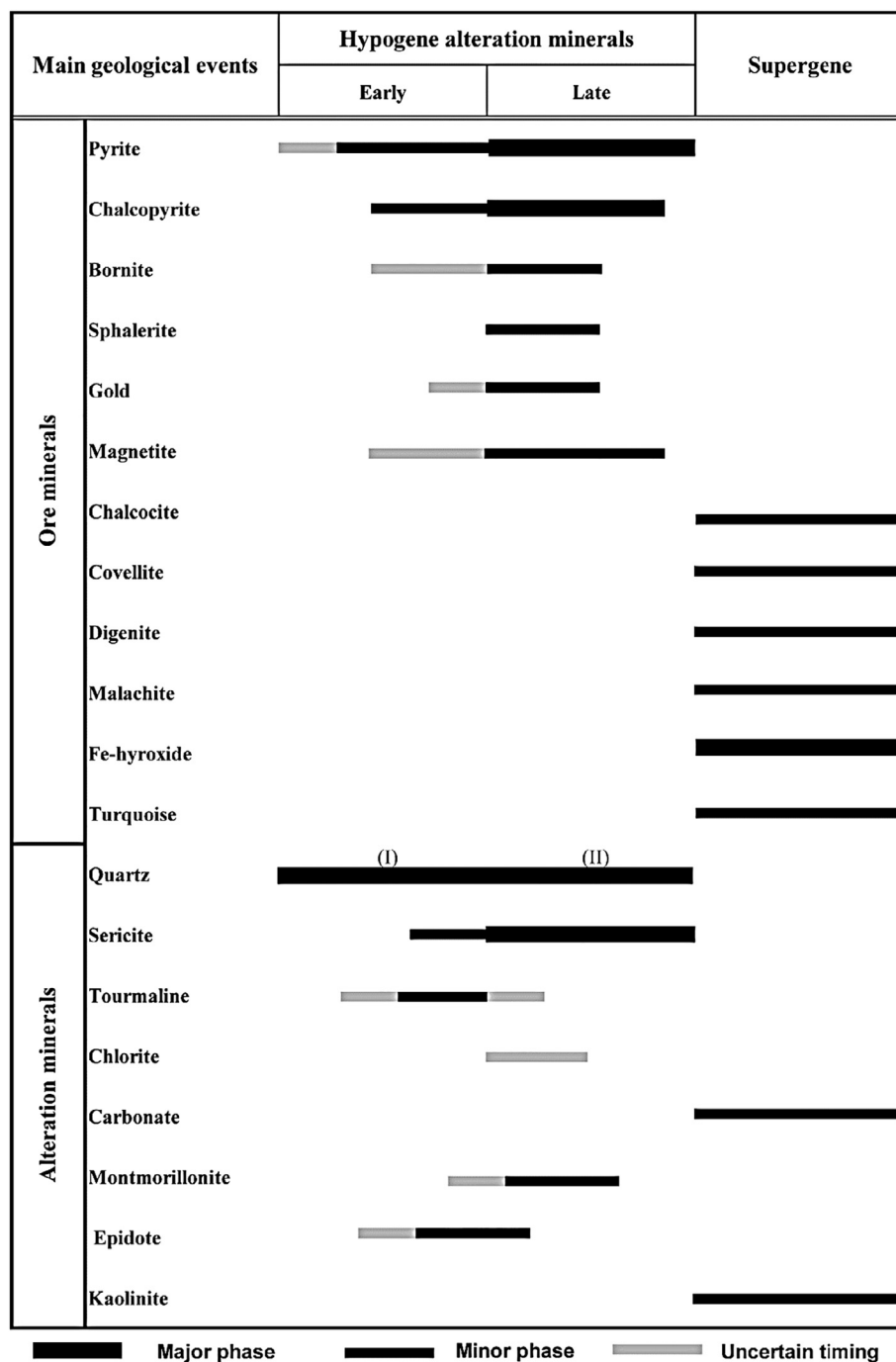


Fig. 13. Paragenetic sequence of ore and alteration minerals in gold – bearing veins of the Baghu gold deposit. I and II refer to stages I and II of the mineralization.

## 8. Discussion

### 8.1. Features of the vein system at the Baghu deposit

Formation of the quartz veins and coeval emplacement of intrusions were the result of a structurally controlled event coincident with fluid migration in the Baghu area. Although a full kinematic analysis has not been done, an analogy to Riedel veins is noted. In this model, the bounding veins parallel the original shear plane, occupying what were initially areas of spaced fracture cleavage. The veins occur in steeply dipping faults implying that the fluid flow was structurally controlled by analogy to Riedel veins. Riedel shear fracturing during oblique convergence in magmatic arcs can develop structures that may host hydrothermal veins or sub-volcanic intrusions (Fedoseev, 2008). This

mechanism had an important role in formation of the Baghu gold-bearing quartz veins. These veins are subparallel and might have formed during extension that was synchronous with pluton emplacement. Formation of this ore deposit was facilitated by the development of a Riedel fracture system in response to regional stresses, thus allowing fluid circulation. These features are similar to those documented in intrusion-related gold systems where vein formation is the result of interplay between ambient stress and high fluid pressure related to I-type granitoids (e.g., Marsh et al., 2003; Stephens et al., 2004; Hart, 2007). Notably, the presence of similar zones of spaced fracture cleavage that are 2–3 m in width, but are non-dilated and vein filled, are still observed in coastal exposures in this area. Thus, locally over-pressured fluids were focused within these structurally prepared areas where extension facilitated vein formation.



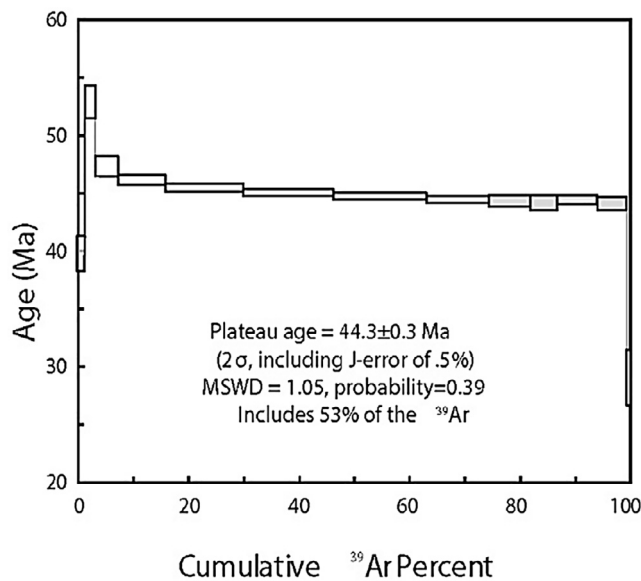


Fig. 14. Parent  $^{40}\text{Ar}/^{39}\text{Ar}$  age spectra for hydrothermal sericite from the quartz-tourmaline gold bearing vein hosted by micro granodiorite in the Baghu deposit.

The Baghu Eocene granitoids form small, shallow, I-type, subduction-related bodies that intrude Eocene volcano-sedimentary units. The intrusions, as well as the volcanic rocks, have arc-like signatures with

calc-alkaline to shoshonitic affinity, including Nb, Ta, and Ti depletion and enrichment in Ba, Rb, U, Pb, and K. Zircon U–Pb SIMS dating of the volcanic unit has yielded an age of  $47.5 \pm 2.4$  Ma (Fig. 8A). Also, a number of subvolcanic cryptodomes and hypabyssal plutons and dikes have yielded ages of  $43.4 \pm 1.3$  Ma and  $38.0 \pm 0.87$  Ma, respectively (Fig. 8B). Fluid exsolution from the different intrusive bodies is responsible for the diversity of hydrothermal alteration assemblages in the deposit area. The epizonal auriferous vein systems in the Baghu deposit are hosted by small Middle Eocene granitic domes.

## 8.2. Hydrothermal alteration and ore-forming fluids

In the Baghu area, the hydrothermal alteration associated with the stage II mineralization in the volcano-plutonic units includes argillic assemblages, phyllic (QSP) assemblages, tourmaline-turquoise, sericite, pyrite, chlorite, and quartz. Oxygen and hydrogen isotope ratios for turquoise suggest mineral precipitation from connate waters (Taghipour and Mackizadeh, 2014).

Several alternative fluid sources have been suggested for the formation of IRGS. The dominant component is magmatic but metamorphic and meteoric fluids could also be important (Lang and Baker, 2001). Probability of involvement of metamorphic fluids increases in settings where magmatic-hydrothermal activity and regional metamorphism are coeval (Moràvek, 1995; Spiridinov, 1996). Magmatic fluids in shallow-level IRGS are characterized by an early immiscible brine and  $\text{CO}_2$ -rich vapor (Sillitoe and Thompson, 1998; Sillitoe, 2008). Late low-salinity, aqueous fluids are more likely to be dominated by meteoric water. Estimates of trapping pressures for ore-forming fluids

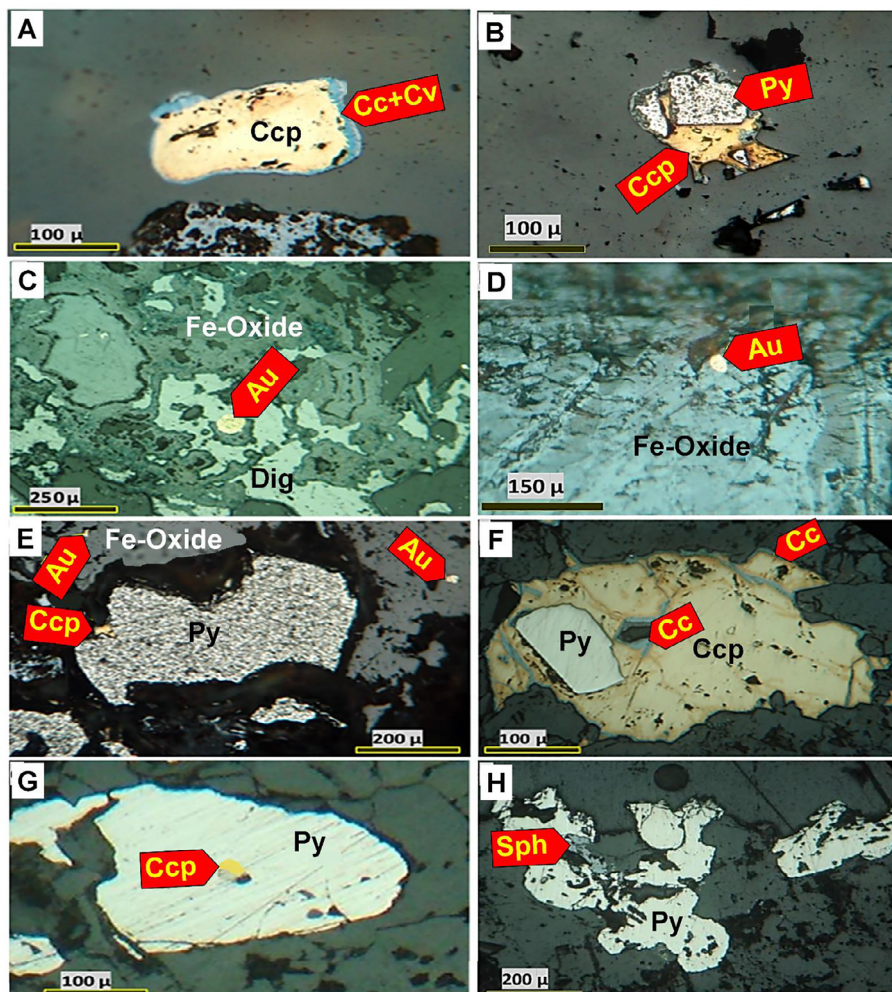
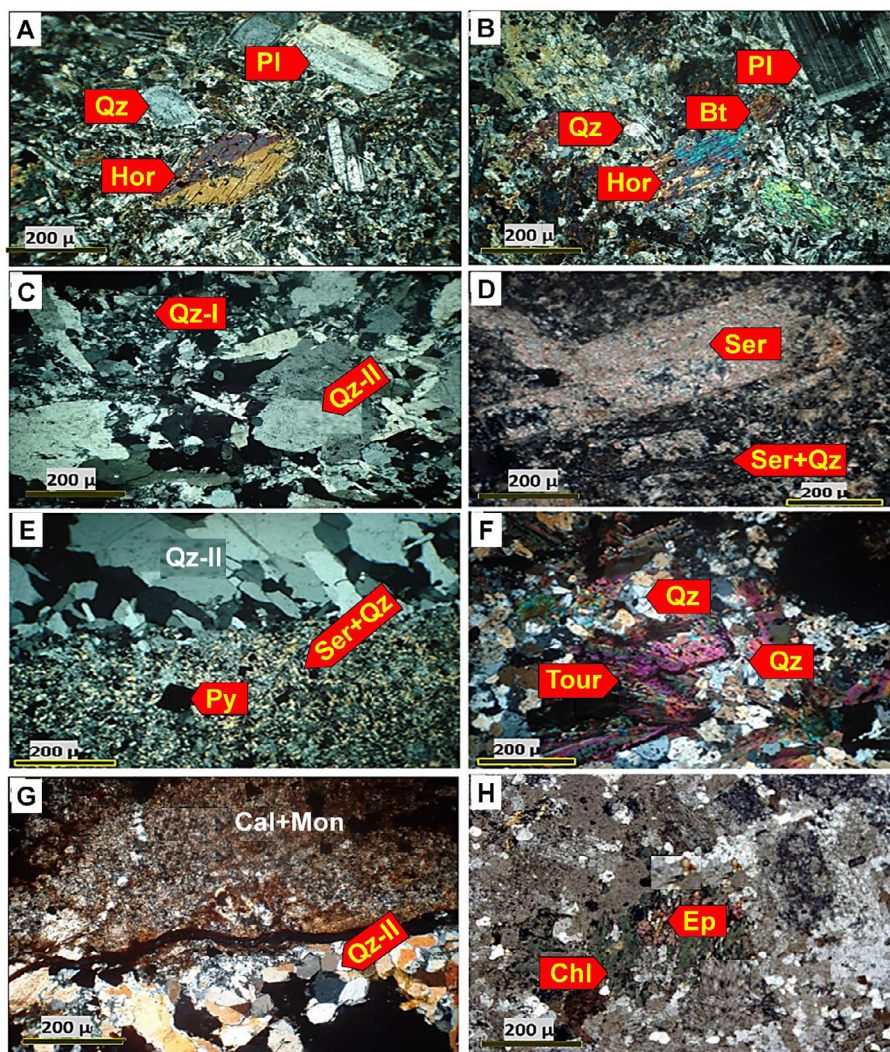


Fig. 15. Reflected-light (RL) photomicrographs (plane-polarized light: PPL) of the stage II ore and gangue vein minerals from the Baghu deposit; (A) chalcopyrite with rim of chalcocite and covellite; (B) chalcopyrite overgrowths on pyrite; (C, D and E) Gold grain in quartz (C), in Fe-oxide resulted from decomposition of pyrite, (D) and Fe-oxide resulted from decomposition of chalcopyrite (E); (F) chalcopyrite overgrowths on pyrite; (G) inclusions of chalcopyrite in pyrite; (H) inclusions of sphalerite in pyrite and along pyrite contact. Abbreviation: Ccp = chalcopyrite, Py = pyrite, Cc = chalcocite, Cv = covellite, Au = gold, Sph = sphalerite, Dig = digenite.





**Fig. 16.** Crossed polarized-light (XPL) photomicrographs of volcano-plutonic rocks and associated alteration from the Baghu gold deposit (A) andesite flow, with prominent brown hornblende and plagioclase phenocrysts, set in a slightly vesicular glassy matrix containing abundant plagioclase crystallites; (B) microgranodiorite porphyry, with hornblende, biotite, quartz and plagioclase phenocrysts, set in matrix with microlithic plagioclase crystallites; (C) two types of quartz: stage I dense microcrystalline quartz that occurs as pervasive alteration of host rocks, and stage II coarse crystalline quartz that grew perpendicular to the walls of the stage I; (D) sericite in the phyllic zone. Plagioclase relicts are sericitized in a groundmass of mainly sericite and quartz; (E) coarse quartz (Qz-II) in above and quartz, sericite and pyrite (opaque) in the below; (F) radial tourmaline growth in a groundmass of quartz; (G) montmorillonite inside of coarse grain quartz (Qz-II) in thin section. Montmorillonite is the dark colored material replacing the feldspars; (H) epidotization and chloritization of plagioclase in granodioritic rocks in the propylitic alteration zone. Abbreviation: Qz-I = quartz stage I, Qz-II = quartz stage II, Ser = sericite, Chl = chlorite, Cal = calcite, Mon = montmorillonite, Ep = epidote, Bt = biotite, Hor = hornblende, Pl = plagioclase, Tour = tourmaline, Py = pyrite. (For interpretation of the references to colour in this figure legend, the reader is referred to the web version of this article.)

at the Baghu deposit were determined using type III and IV inclusions and the methodology described by Touret and Dietvorst (1983).

Calculated values (using Zheng, 1993) for  $\delta^{18}\text{O}$  fluid range between approximately 8.0 and 10.3 per mil, indicative of an isotopically heavy crustal fluid and likely little involvement of meteoric water, even at epizonal crustal levels. Our results suggest the involvement of a magmatic fluid in the hydrothermal system. However, it is impossible to directly link the hydrothermal system in time with a specific magmatic event.

Sulfur isotope ratios for pyrite and chalcopyrite from the gold-bearing veins range from +1.5 to +3.1 per mil. The narrow distribution of these data suggest that sulfur was derived either directly from a high temperature, reduced magmatic source, or through leaching of volcanic and plutonic country rocks yielding  $\text{H}_2\text{S}$ -bearing fluids. According to Hofstra and Cline (2000) and Emsbo and Hofstra (2003),  $\delta^{34}\text{S}$  values of about +2.5 per mil are interpreted to indicate oxidation of magmatic  $\text{H}_2\text{S}$  during reducing conditions in hydrothermal fluids. These results are consistent with fluid inclusions studies in the auriferous vein systems at Baghu, where metal precipitation resulted from a decrease in gold solubility during fluid immiscibility, and cooling and crystallization of multiphase-bearing inclusions.

### 8.3. Ligands and redox conditions

High-salinity fluids show that chloride is a dominant ligand for mobilizing numerous metals in aqueous solutions at the Baghu Au

deposit. According to Gammons and Williams-Jones (1997), magmatic fluids that evolve from shallow intrusion bodies, such as those in the Baghu area, tend to boil shortly after leaving the melt. At such a point, most of the dissolved gold will partition along with chloride into the brine phase, although Williams-Jones and Heinrich (2005) note that under some conditions the opposite is possible.

The high salinities of the type V inclusions can be explained by degassing or unmixing from a  $\text{CO}_2$ -rich fluid (e.g., Cline and Bodnar, 1994; Dugdale and Hagemann, 2001; Baker, 2002; Hagemann and Luders, 2003; Evans et al., 2008; Jaguin et al., 2014; Hao et al., 2015). The  $\text{CO}_2$  is documented in the Baghu fluid inclusions, and the wide range in fluid inclusion homogenization temperatures is perhaps the result of variation in the trapping pressures. Therefore, liquid-vapor immiscibility preferentially partitions the anomalous copper in the Baghu deposit into the high-salinity liquid phase (Candela and Holland, 1986). Higher Cl concentrations in aqueous fluids can promote greater cation solubilities, particularly for alkali species (Na, K, Rb) (e.g., Candela and Holland, 1986). Kesler et al. (2002) showed that gold is mobile in highly oxidizing, Cl-rich waters typical of intrusion-related gold-copper systems. However, at high  $f\text{O}_2$  values,  $\text{H}_2\text{S}$  is oxidized to  $\text{SO}_2$ , which clearly decreases gold mobility as a bisulfide complex. Thus, strongly oxidizing conditions will favor transport of gold and base metals as chloride complexes at all temperatures (Gammons and Williams-Jones, 1997; Asadi et al., 2013a and b; Asadi et al., 2015).

The relationship between fluid  $\text{CO}_2$  content and ore grade is uncertain, and  $\text{CO}_2$  appears to play no significant role in the Au



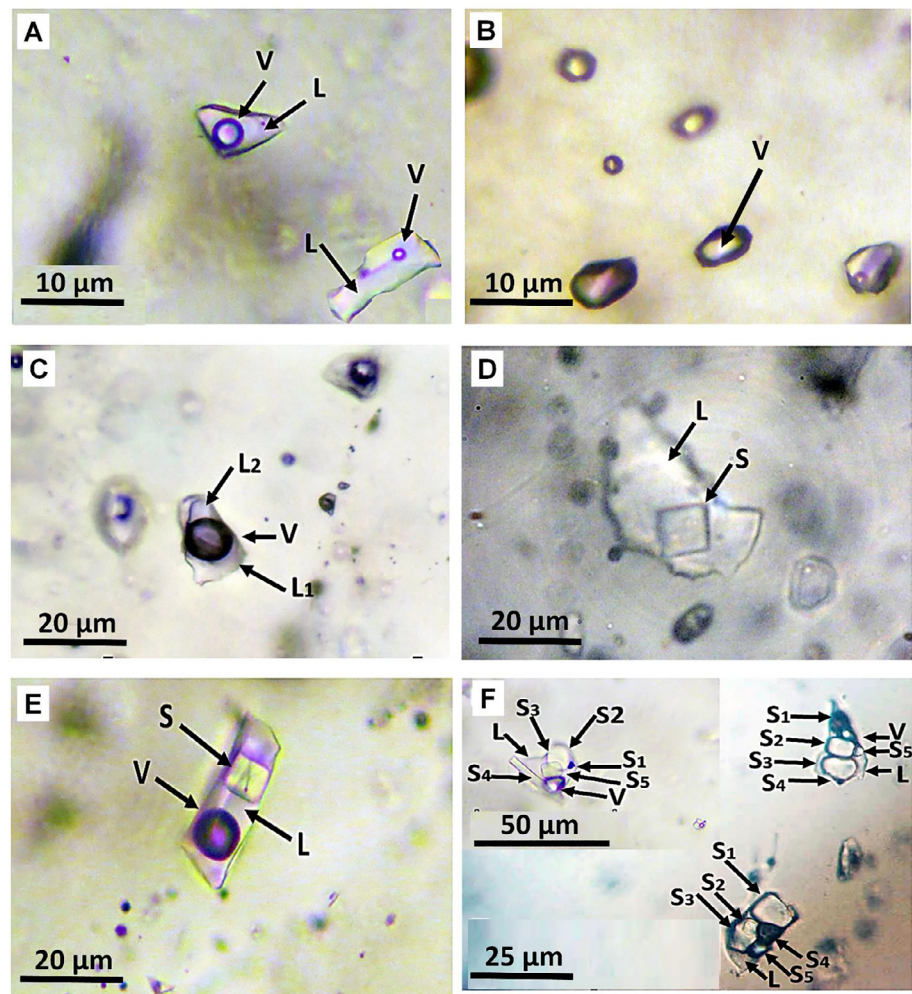


**Fig. 17.** Fluid inclusion in quartz II. All measurements were on inclusions in the gold bearing quartz vein (A) type III – Two-phase aqueous and gaseous inclusions; (B) type II – one-phase gaseous inclusions; (C) type IV – three-phase carbonic-aqueous inclusions; (D) type VI two-phase liquid and solid (halite) inclusions; (E) and (F) type VII and VIII – hypersaline liquid, multi-phase solid and gas (aqueous liquid + vapor + halite ± sylvite ± mica ± anhydrite? ± boric acid [H<sub>3</sub>BO<sub>3</sub>] + opaque mineral such as pyrite, chalcocopyrite and hematite).

precipitation process (Hofstra and Cline, 2000). Cline et al. (2005) have shown that ore-forming fluids were low- to moderate-temperature (~180–350 °C), moderate-salinity (~5–10 wt% NaCl eqv) aqueous fluids that contained CO<sub>2</sub>, and sufficient SO<sub>2</sub> (formed by oxidation of H<sub>2</sub>S) to have precipitated gold and other metals in the veins. The main stage of Au mineralization is related to the stage II quartz veins, where inclusions show evidence of fluid immiscibility.

Also, salts of Cl<sup>-</sup>, SO<sub>4</sub><sup>2-</sup>, and CO<sub>3</sub><sup>2-</sup>, such as KCl, CaSO<sub>4</sub>, and Na<sub>2</sub>CO<sub>3</sub>, have significantly greater solubilities in aqueous fluids than do silicates, and consequently greater amounts of these materials can be transported by hydrothermal fluids. Thus carbonates, halides, and sulfates are

commonly found in fluid inclusions. In this study, chloride is a dominant ligand for mobilizing numerous metals in aqueous solutions (Fig. 19).

8.4. Saline fluid flow and rock permeability

The interplay between saline fluid flow and rock permeability controls the ore mineralization. Precipitation of halite from high-salinity magmatic-hydrothermal fluids might restrict fluid flow (Sanchez et al., 2015). This is because NaCl crystals may reduce permeability by filling the pore spaces (e.g., Hesshaus et al., 2013) in the country rock

**Table 3**  
Microthermometric data of primary fluid inclusions in the Baghu quartz veins (stage-II).

Inclusion types	Phase	Number	T <sub>m</sub> (Halite) = T <sub>m</sub> (s <sub>1</sub> ) and (s <sub>2</sub> ) (°C)	T <sub>m</sub> (CO <sub>2</sub> ) (°C)	T <sub>m</sub> (Ice) (°C)	T <sub>m</sub> (Cla) (°C)	Th(CO <sub>2</sub> ) (°C)	Th(°C)	Salinity (wt% NaCl equiv.)	Pressure (MPa)
III	L + V	136			-15.1 to -0.5			180–312	0.50–15.67	
IV	L1 + L <sub>2</sub> + V	38		-61.0 to -56.3		3.1–8.5	23.8–30.4	220.3–382.2	3.80–11.20	98.1–132.4
V	L + V + S	118	198 to 490					235–590.3	33.49–52.47	

T<sub>m</sub>(Ice): final ice melting temperature; T<sub>m</sub>(Cla): dissolution temperature of CO<sub>2</sub> clathrate; T<sub>m</sub>(CO<sub>2</sub>): melting temperature of CO<sub>2</sub> phase; Th(CO<sub>2</sub>): homogenization temperature of CO<sub>2</sub> phase into the carbonic vapor phases; T<sub>m</sub>(Halite): dissolution temperature of halite (s<sub>1</sub>) and sylvite (s<sub>2</sub>); and Th: homogenization temperature. Fluid inclusion terminology and symbols according to Diamond (2003b).

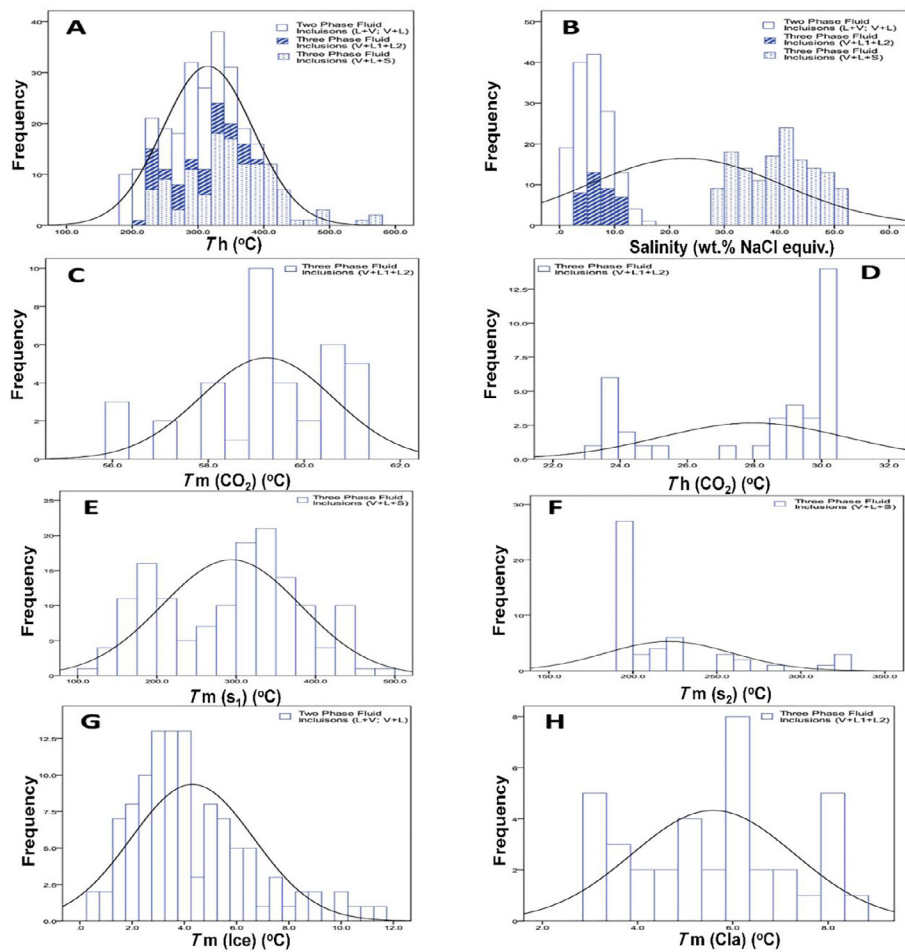


**Fig. 18.** Histograms of fluid inclusions in gold bearing quartz veins (A) histograms of homogenization temperatures ( $T_h$ ) (°C); (B) salinities (wt% NaCl equivalent); (C)  $\text{CO}_2$  melting temperature ( $T_{m(\text{CO}_2)}$ ) (°C); (D)  $\text{CO}_2$  homogenization temperature ( $T_h(\text{CO}_2)$ ) (°C); (E) halite dissolution temperature ( $T_{m(\text{Halite})} = T_{m(s_1)}$ ) (°C); (F) sylvite dissolution temperature ( $T_{m(\text{Halite})} = T_{m(s_2)}$ ) (°C); (G) ice melting temperature ( $T_{m(\text{Ice})}$ ) (°C); (H) Clathrate melting temperature ( $T_{m(\text{Cla})}$ ) (°C). Fluid inclusion terminology and symbols according to [Diamond \(2003b\)](#).

**Table 4**  
Oxygen isotope values (per mil) of gold-bearing quartz veins.

Sample	Mineral	$\delta^{18}\text{O}_{\text{quartz}}$	$\delta^{18}\text{O}_{\text{fluid}}$	Locations UTM (WGS84)
B1	Quartz	11.6	8	0287549 E 3926164 N
B3	Quartz	11.6	8	0287549 E 3926164 N
B4	Quartz	11.7	8.1	0287565 E 3926148 N
B5	Quartz	11.7	8.1	0287631 E 3926081 N
B7	Quartz	12.9	9.3	0287443 E 3926254 N
B8	Quartz	12.9	9.3	0287518 E 3926127 N
B9	Quartz	13.1	9.5	0287180 E 3925924 N
B11	Quartz	13.2	9.6	0287928 E 3926544 N
B6	Quartz	13.3	9.7	0287368 E 3926223 N
B16	Quartz	13.9	10.3	0287162 E 3925910 N

**Table 5**  
Sulfur isotopic compositions of pyrite and chalcopryite from the Baghu gold deposit (per mil).

Sample	Delta $^{34}\text{S}_{\text{CDT}}$	UTM(WGS84)
B1	1.5	0287549 E 3926164 N
B3	1.6	0287559 E 3926191 N
B4	1.6	0287565 E 3926148 N
B5	1.6	0287631 E 3926081 N
B6	1.7	0287368 E 3926223 N
B7	1.8	0287443 E 3926254 N
B8	2.2	0287518 E 3926127 N
B9	2.6	0287180 E 3925924 N
B10	2.6	0287181 E 3925933 N
B11	2.9	0287928 E 3926544 N
B13	3.1	0287162 E 3925910 N



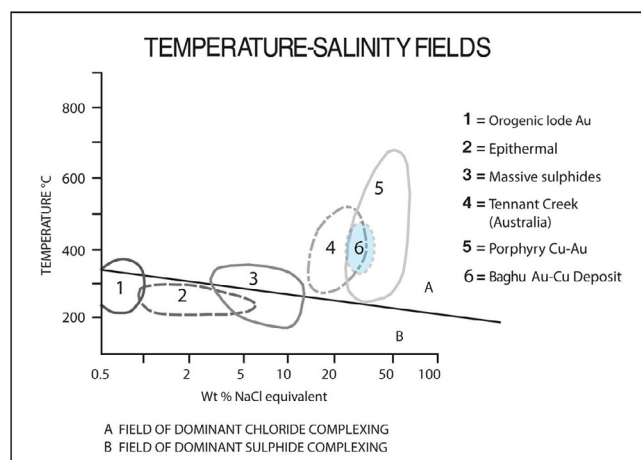


**Fig. 19.** Temperature-salinity fields and mean gradient curve for a range of hydrothermal ore systems: (1) Archaean orogenic Au; (2) Epithermal Au-Ag; (3) volcanogenic massive sulfides; (4) Tennant Creek Au-Cu, Australia; (5) Porphyry Cu-Au; (6) Baghu Au-Cu deposit. After Large et al. (1988).

on time scales of tens to thousands of years (Weis, 2015). Alternatively, precipitation of halite, quartz, and other solid phases may lead to episodic fluid pressure increase and subsequent hydraulic fracturing (Weis, 2015). The resulting fracture-enhanced permeability controls fluid flow and ore precipitation.

As a fluid traverses the phase boundary from liquid-vapor stability toward vapor-halite stability, the mass fraction of liquid decreases abruptly, and the capacity of the aqueous phase to carry copper is reduced. Salt saturation in the Baghu magmatic-hydrothermal system may thus act as a direct precipitation mechanism of base metal-bearing chlorides (Gruen et al., 2014). The coexisting vapor phase, which ascends rapidly, would transport sulfur and gold upward. This precipitation mechanism is limited by the availability of reduced sulfur, which depends on behavior of  $\text{SO}_2$  as the magmatic fluid ascends. At relatively low pressure, disproportionation of  $\text{SO}_2$  is likely to occur at temperatures above or close to the conditions of halite saturation, providing reduced sulfur for sulfide precipitation (Seal, 2006). Fluid inclusion data from porphyry deposits worldwide (e.g., Candela and Holland, 1986; Gammons and Williams-Jones, 1997; Jugo et al., 1999; Ulrich et al., 2001; Kouzmanov and Ramboz, 2003), numerical simulations, and thermodynamic considerations are all consistent with halite saturation and precipitation of solid salt in magmatic-hydrothermal systems associated with upper crustal plutons.

#### 8.5. Behavior of sulfur in the granitoid magma

The behavior of sulfur in granitoid magmas is very important in understanding the metallogeny of intrusion-related gold (and copper) ore deposits (Frank et al., 2011; Wallace and Edmonds, 2011). High concentrations of Cu and Au within sulfur-rich calc-alkaline magmas characterizes subduction zone intrusion-related ore deposits (Yang, 2012). Gold and associated metallic elements in the Baghu IRGD may therefore be directly derived from a causative intrusion, although minor amounts could be incorporated from country rocks by selective assimilation and subsequent fractional crystallization. Jugo et al. (1999) show that gold partition coefficients for an intermediate solid solution (Iss) and pyrrhotite (Po) are, respectively,  $D^{\text{Iss/melt}}(\text{gold}) = 5.7 \times 10^3$  and  $D^{\text{Po/melt}}(\text{gold}) = 140$ , indicating that fractional crystallization of sulfide melt gradually deplete a granitic melt in chalcophile metals. This result is consistent with observations from granitoid rocks at the Baghu deposit. Furthermore,  $D^{\text{Po/melt}}(\text{gold})$  may greatly increase with increasing  $f(\text{S}_2)$  and decreasing  $f(\text{O}_2)$  within the pyrrhotite stability field. Destabilization of both magmatic Iss and Po relative to magnetite due to changes in  $f(\text{O}_2)$  and  $f(\text{S}_2)$ . This could have led to the release of

gold from sulfides to the melt and/or magmatic fluids and provided a source of metals and sulfur to ore-forming fluids in the Baghu deposit.

## 9. Conclusions

The Baghu intrusion-related gold deposit is spatially related to middle Eocene hypabyssal calc-alkaline microgranite and granodiorite porphyry stocks that were emplaced during Neotethys subduction. The high-level emplacement of the intrusions in the TMA was controlled by the regional extensional regime that was later overprinted by an ENE-striking, strike-slip fault system. An ion-probe U-Pb zircon age of  $43.4 \pm 1.3$  Ma for the Baghu felsic subvolcanic rocks overlaps the  $^{40}\text{Ar}/^{39}\text{Ar}$  sericite age of  $44.3 \pm 0.3$  Ma for the gold-related magmatic-hydrothermal event. The overlapping ages indicate a short life span for the magmatic-hydrothermal system, which is consistent with the relatively simple history and shallow depth of the intrusive system. The presence of magnetite in the ore assemblage and the fluid inclusion data suggest an “oxidized” affiliation of the gold deposit.

Fluid inclusion data exhibit a positive correlation between salinity and homogenization temperature, with quartz veins forming at higher temperature having more saline fluids. Based on the criteria of workers such as Lowenstern (2001) and Asadi et al. (2013b, 2014, 2017), degassing of  $\text{CO}_2$  from a  $\text{CO}_2$ -rich magma and a high ratio of  $\text{CO}_2/\text{H}_2\text{O}$  in fluids would result in a low NaCl activity in the initial ore-forming fluids, causing paucity of halite-bearing inclusions as was observed in our main stage hydrothermal quartz veins (cf. Baker, 2002). The  $\text{CO}_2/\text{H}_2\text{O}$  ratio typically decreased during progressive decompression or crystallization-induced degassing. Such a process could occur during fluid immiscibility due to the partitioning of acidic components (e.g.,  $\text{CO}_2$ , and  $\text{SO}_2$ ) into the vapor phases, thereby increasing the  $\text{H}_2\text{O}/\text{CO}_2$  ratio, while decreasing  $\text{HCO}_3^-$  and  $\text{CO}_3^{2-}$  contents, causing a drop in Eh (and a rise in pH and ion concentration) that facilitated the precipitation of sulfide minerals (see Drummond and Ohmoto, 1985). Therefore, the escape of  $\text{CO}_2$  was an important factor in increasing the activity of NaCl and  $\text{S}^{2-}$ , and precipitation of halite in fluid inclusions and ore minerals at shallow crustal levels at Baghu.

The S isotope values for the gold-related pyrite and chalcopyrite suggest that sulfur was derived either directly from a magmatic source, or through leaching of volcanic and plutonic country rocks. The calculated  $\delta^{18}\text{O}$  values of fluids in equilibrium with the vein quartz are also consistent with a magmatic source. Based on the scenario, we argue the ore-forming metals were derived from the lower crust with also addition of mantle material. The evidence presented here suggests that the Baghu deposit is related to magmatic-hydrothermal activity associated with the intrusion of the microgranodioritic body.

## Conflict of interest

We confirm that there are no known conflicts of interest associated with this publication. The manuscript is an original work. This manuscript has not been published in whole or in part, nor is it being considered for publication elsewhere. We also confirm that all the listed authors have participated actively in the study, and have seen and approved the submitted manuscript. The authors do not have any possible conflicts of interest.

## Acknowledgments

This study was funded by the Geological Survey of Iran (GSI). Thanks are also extended to the University of Tehran – Iran for various supports. We would like to extend our thanks to Prof. Richard Goldfarb and Prof. David Lentz for critically reading the manuscript and English corrections. Thanks is also extended to Dr. Ryan Taylor at the USGS for Ar-Ar and stable isotope analyses. The U-Pb data acquisition at UCLA was supported by the Caltech Tectonics Observatory under the auspices of Gordon and Betty Moore Foundation – United States. The ion

microprobe facility at UCLA – United States, is partly supported by a grant from the Instrumentation and Facilities Program, Division of Earth Sciences, National Science Foundation – United States.

## References

- Agard, P., Omrani, J., Jolivet, L., Mouthereau, F., 2005. Convergence history across Zagros (Iran): constraints from collisional and earlier deformation. *Int. J. Earth Sci.* 94, 401–419.
- Ahlgren, S.G., 2001. The nucleation and evolution of Riedel shear zones as deformation bands in porous sandstone. *J. Struct. Geol.* 23, 1203–1214.
- Alavi, M., 1991. Sedimentary and structural characteristics of the Paleo-Tethys remnants in northeastern Iran. *Geol. Soc. Am. Bull.* 103, 983–992.
- Asadi, S., 2013. Geochemistry of selected productive and barren intrusions in Shahr Babak copper complex, Urumiyeh–Dokhtar volcano-magmatic belt (Ph.D. thesis). Shiraz University, Iran, pp. 283.
- Asadi, S., Mathur, R., Moore, F., Zarasvandi, A., 2015. Copper isotope fractionation in the Meiduk porphyry copper deposit, Northwest of Kerman Cenozoic magmatic arc. *Iran. Terra Nova* 27, 36–41.
- Asadi, S., Moore, F., Fattahi, N., 2013a. Fluid inclusion and stable isotope constraints on the genesis of the Jian copper deposit, Sanandaj–Sirjan metamorphic zone. *Iran. Geofluids* 13, 66–81.
- Asadi, S., Moore, F., 2017. Fluid evolution in H<sub>2</sub>O–CO<sub>2</sub>–NaCl system and metallogenic analysis of the Surian metamorphic complex, Bavanat Cu deposit, southwest Iran. *Miner. Petrol.* 111, 145–161.
- Asadi, S., Moore, F., Zarasvandi, A., 2014. Discriminating productive and barren porphyry copper deposits in the southeastern part of the central Iranian volcano-plutonic belt, Kerman region, Iran: a review. *Earth-Sci. Rev.* 138, 25–46.
- Asadi, S., Moore, F., Zarasvandi, A., Kosrojerdi, M., 2013b. First report on the occurrence of CO<sub>2</sub>-bearing fluid inclusions in Meiduk porphyry copper deposits, Iran: Implications for mineralizing processes in a continental collision setting. *Geologos* 13, 66–81.
- Ashrafpour, E., Ansdell, K.M., Alirezaei, S., 2012. Hydrothermal fluid evolution and ore genesis in the Arghash epithermal gold prospect, northeastern Iran. *J. Asian. Earth. Sci.* 51, 30–44.
- Asiabanha, A., Bardintzeff, J.M., Kananian, A., Rahimi, G., 2012. Post-Eocene volcanics of the Abazar district, Qazvin, Iran: mineralogical and geochemical evidence for a complex magmatic evolution. *J. Asian. Earth. Sci.* 45, 79–94.
- Babakhani, A., Mehrpartu, M., Radfar, J., 1996. Geological map in 1:20000 scale with exploration report of Kuhzar deposit. *Geol. Surv. Iran*.
- Baker, T., 2002. Emplacement depth and carbon dioxide-rich fluid inclusions in intrusion-related gold deposits. *Econ. Geol.* 97, 1111–1117.
- Bakker, R.J., 1999. Optimal interpretation of microthermometrical data from fluid inclusions: thermodynamic modeling and computer programming (Ph.D. thesis). Ruprecht-Karls University, Germany, pp. 50.
- Bakker, R.J., 1997. Clathrates: computer programs to calculate fluid inclusion V-X properties using clathrate melting temperatures. *Comput. Geosci.* 23, 1–18.
- Berberian, M., King, G.C.P., 1981. Towards a paleogeography and tectonic evolution of Iran. *Canadian Journal of Earth Sciences* 18 (2), 210–265.
- Bodnar, R.J., 1993. Revised equation and table for determining the freezing point depression of H<sub>2</sub>O–NaCl solutions. *Geochim. Cosmochim. Acta* 57, 683–684.
- Bowers, T.S., Helgeson, H.C., 1983. Calculation of the thermodynamic and geochemical consequences of nonideal mixing in the system H<sub>2</sub>O–CO<sub>2</sub>–NaCl on phase relations in geological systems: equation of state for H<sub>2</sub>O–CO<sub>2</sub>–NaCl fluids at high pressures and temperatures. *Geochim. Cosmochim. Acta* 47, 1247–1275.
- Boynton, W.V., 1984. Cosmochemistry of the rare earth elements: meteorite studies. In: Henderson, P. (Ed.), *Rare Earth Element Geochemistry*. Elsevier, Amsterdam, pp. 63–114.
- Brown, P.E., 1989. Flincor: a microcomputer program for the reduction and investigation of fluid inclusion data. *Am. Mineral.* 74, 1390–1393.
- Brown, P.E., Hagemann, S.G., 1994. MacFlinCor: a computer program for fluid inclusion data reduction and manipulation. Fluid inclusions in minerals: methods and applications. Virginia Polytechnic Institute and State University, Blacksburg VA, pp. 231–250.
- Burgess, R., Kiviets, G.B., Harris, J.W., 2004. <sup>40</sup>Ar/<sup>39</sup>Ar age determinations of eclogitic clinopyroxene and garnet inclusions in diamonds from the Venetia and Orapa kimberlites. *Lithos* 77, 113–124.
- Candela, P.A., Holland, H.D., 1986. A mass-transfer model for copper and molybdenum in magmatic hydrothermal systems; the origin of porphyry-type ore deposits. *Econ. Geol.* 81, 1–19.
- Cline, J.S., Hofstra, A.H., Tosdal, R.M., Muntean, J., Hickey, K.A., 2005. Carlin-type gold deposits in Nevada, USA: critical geologic characteristics and viable models. *Econ. Geol.* 100, 451–484.
- Cline, J.S., Bodnar, R.J., 1994. Direct evolution of a brine from crystallizing silicic melt at the Questa, New Mexico, molybdenum deposit. *Econ. Geol.* 89, 1780–1802.
- Compston, W., Williams, I.S., Meyer, C., 1984. U–Pb geochronology of zircons from Lunar Breccia 73217 using a sensitive, high mass resolution ion microprobe. *J. Geophys. Res.* 89, 8525–8534.
- Davis, G.H., Bump, A.P., Garcia, P.E., Ahlgren, S.G., 1999. Conjugate Riedel deformation band shear zones. *J. Struct. Geol.* 22, 169–190.
- Dercourt, J., Ricou, L.E., Vrielynck, B., 1993. Atlas Tethys Palaeoenvironmental maps, Atlas of Tethys Project (14 maps), Report Series 1 (Paris). Inst. français du pétrole.
- Dercourt, J., Zonenshain, L.P., Ricou, L.E., Kazmin, V.G., Le, Pichon, X., Knipper, A.L., Grandjacquet, C., Shorshikov, I.M., Geyssant, J., Lepvrier, C., Pechevsky, D.H., Boulou, J., Sibuet, J.C., Savostin, L.A., Sorokhtin, O., Westphal, M., Bazhenov, M.L., Lauer, J.P., Biju-Duval, B., 1986. Geological evolution of the Tethys belt from the Atlantic to the Pamirs since the Lias. *Tectonophysics* 123, 241–315.
- Diamond, L.W., 2003a. Systematics of H<sub>2</sub>O inclusions in fluid inclusions. In: Samson, I.M., Anderson, A.G., Marshall, D.D. (Eds.), *Fluid Inclusions: Analysis and Interpretation*. Mineral. Assoc. Can, Vancouver, pp. 55–79.
- Diamond, L.W., 2003b. Glossary: Terms and symbols used in fluid inclusion studies. In: Samson, I.M., Anderson, A.G., Marshall, D.D. (Eds.), *Fluid Inclusions: Analysis and Interpretation*. Mineral. Assoc. Can, Vancouver, pp. 363–372.
- Dreher, A.M., Xavier, R.P., Taylor, B.E., Martini, S., 2007. New geologic, fluid inclusion and stable isotope studies on the controversial Igarapé Bahia Cu–Au deposit, Carajás Province, Brazil. *Miner. Deposita* 43, 161–184.
- Drummond, S.E., Ohmoto, H., 1985. Chemical evolution and mineral 'deposition' in boiling hydrothermal systems. *Econ. Geol.* 80, 126–147.
- Dugdale, A.L., Hagemann, S.G., 2001. The Bronzewing lode-gold deposit, Western Australia: P–T–X evidence for fluid immiscibility caused by cyclic decompression in gold-bearing quartz veins. *Chem. Geol.* 173, 59–90.
- Emsbo, P., Hofstra, A.H., 2003. Origin and significance of post dissolution collapse breccias cemented with calcite and barite at the Meikle gold deposit, northern Carlin trend, Nevada. *Econ. Geol.* 98, 1243–1252.
- Evans, M.J., Derry, L.A., France-Lanord, C., 2008. Degassing of metamorphic carbon dioxide from the Nepal Himalaya. *Geochim. Geophys. Geosyst.* 9 (4).
- Fard, M., Rastad, E., Ghaderi, M., 2006. Epithermal gold and base metal mineralization at Gandy, north of Central Iran and the role of rhyolitic intrusions. *J. Sci. Islam. Republ. Iran* 17, 327–335.
- Fedoseev, G.S., 2008. The role of mafic magmatism in age specification of Devonian continental trough deposits: evidence from the Minusa Basin, western Siberia, Russia. *Bull. Geosci.* 83, 473–480.
- Frank, M.R., Simon, A.C., Pettke, T., Candela, P.A., Piccoli, P.M., 2011. Gold and copper partitioning in magmatic-hydrothermal systems at 800 °C and 100 MPa. *Geochim. Cosmochim. Acta* 75, 2470–2482.
- Gammons, C.H., Williams-Jones, A.E., 1997. Chemical mobility of gold in the porphyry-epithermal environment. *Econ. Geol.* 92, 45–59.
- Ghasemi, A., Talbot, C.J., 2006. A new tectonic scenario for the Sanandaj–Sirjan Zone (Iran). *J. Asian Earth. Sci.* 26, 683–693.
- Ghasemi, H., Jamshidi, Kh., Sadeghian, M., 2014. Petrology and geochemistry of the Sabzevar post-ophiolitic high silica adakitic rocks. *Petrology* 17, 51–68.
- Ghorbani, G., Abedini, M. V., Ghasemi, H., 2006. Petrology of Granitoid Rocks from south of Damghan, Northern Iran. The 6th International Conference on the Geology of the Middle East. UAE University. Al Ain, UAE.
- Goldstein, R.H., 2003. Petrographic analysis of fluid inclusions. *Fluid Incl. Anal. Interpret.* 32, 9–53.
- Gruen, G., Weis, P., Driesner, T., Heinrich, C.A., Ronde, C.E.J., 2014. Hydrodynamic modeling of magmatic-hydrothermal activity at submarine arc volcanoes, with implications for ore formation. *Earth Planet. Sci. Lett.* 404, 307–318.
- Hagemann, S.G., Lunders, V., 2003. P–T–X conditions of hydrothermal fluid and precipitation mechanism of stibnite-gold mineralization at the Wiluna lode-gold deposits, Western Australia: conventional and infrared microthermometric constraints. *Miner. Deposita* 38, 936–952.
- Hall, D.L., Sterner, S.M., Bodnar, R.J., 1988. Freezing point depression of NaCl–KCl–H<sub>2</sub>O solutions. *Econ. Geol.* 83, 197–202.
- Hao, Y.J., Ren, Y.S., Yang, Q., Duan, M.X., Sun, Q., Fu, L.C., Li, C., 2015. Ore genesis and formation age of the Gaogangshan Mo deposit, Heilongjiang province, NE China. *Resour. Geol.* 65, 177–192.
- Hart, C., 2007. Reduced intrusion-related gold deposits. In: Goodfellow, W.D. (Ed.), *Mineral Deposits of Canada*. Geol. Assoc. Can, Quebec, pp. 95–112.
- Hart, C.J.R., Goldfarb, R.J., Lewis, L.L., Mair, J.L., 2004. The Northern Cordillera Mid-Cretaceous plutonic Province: ilmenite/magnetite-series granitoids and intrusion-related mineralization. *Resour. Geol.* 54, 253–280.
- Hart, C.J.R., Mair, J.L., Goldfarb, R.J., Groves, D.I., 2005. Source and redox controls of intrusion-related metallogeny, Tombstone-Tungsten Belt, Yukon, Canada: transactions of the Royal Society of Edinburgh. *Earth Sci.* 95, 339–356.
- Helmhacker, R., 1898. Die nutzbaren layerstaten Persians. *Prakt. Sankt Augustin*.
- Hencke, L., 1899. Die Bodenachatzte Persians. *Berg-Hutten- e. Salinen Wasen* 47, 272–274.
- Hesshaus, A., Houben, G., Kringel, R., 2013. Halite clogging in a deep geothermal well; geochemical and isotopic characterization of salt origin. *Phys. Chem. Earth.* 64, 127–139.
- Hofstra, A.H., Cline, J.S., 2000. Characteristics and models for Carlin type gold deposits. *Rev. Econ. Geol.* 13, 163–220.
- Holloway, J.R., 1981. Composition and volumes of supercritical fluids in the Earth crust. In: Hollister, L.S., Crawford, M.L. (Eds.), *Fluid Inclusions: Applications to Petrology*. Mineral. Assoc., Can, Calgary, pp. 13–38.
- Houshmandzadeh, A.R., Alavi Naini, M., Haghighpour, A.A., 1978. Evolution of geological phenomenon in Torud area. Report of Torud geological map Scale 1: 2,50,000. (Report No. H5). Geol. Surv. Iran, Tehran.
- IMIDRO (Iranian Mines and Mining Industries Development and Renovation), 2005. The geology and gold estimation in Kuhzar gold mine, sought Damghan. Imidro Press, Tehran.
- Ishihara, S., 1977. The magnetite-series and ilmenite-series granitic rocks. *Min. Geol.* 27, 293–305.
- Ishihara, S., 1981. The granitoid series and mineralization. *Econ. Geol.* 75, 458–484.
- Ishihara, S., 2004. The redox state of granitoids relative to tectonic setting and earth history: The magnetite–ilmenite series 30 years later. *Trans. R. Soc. Edinburgh: Earth Sci.* 95, 23–33.
- Jaguin, J., Boulvais, P., Boiron, M.C., Poujol, M., Gapais, D., Ruffet, G., Briant, N., 2014. Stable isotopes (O, C) and fluid inclusion study of quartz–carbonate veins from the antimony line, Murchison Greenstone Belt. *Am. J. Sci.* 314, 1140–1170.
- Jourdan, F., Verati, C., Féraud, G., 2006. Intercalibration of the Hb3gr 40 Ar/39 Ar dating standard. *Chem. Geol.* 231 (3), 177–189.
- Jugo, P.J., Candela, P.A., Piccoli, P.M., 1999. Magmatic sulfides and Au:Cu ratios in porphyry deposits: An experimental study of copper and gold partitioning at 850 °C, 100 MPa in a haplogranitic melt–pyrrhotite–intermediate solid solution–gold metal assemblage, at gas saturation. *Lithos* 46, 573–589.

- Katz, Y., Weinberger, R., Aydin, A., 2004. Geometry and kinematic evolution of Riedel shear structures, Capitol Reef National Park, Utah. *J. Struct. Geol.* 26, 491–501.
- Keynezhad, A., Pourkermani, M., Arian, M., Saeedi, A., Lotfi, M., 2010. Research on fractures in North of the Torud – Moaleman area (Central Iran, Southeastern of Damghan) and their relation with mineralization. *Q. J. Earth* 2, 81–97.
- Kesler, S.E., Chrysosoulis, S.L., Simon, G., 2002. Gold in porphyry copper deposits: its abundance and fate. *Ore Geol. Rev.* 21 (1), 103–124.
- Kouzmanov, K., Ramboz, C., 2003. Stable isotopic constraints on the origin of epithermal Cu–Au and related porphyry copper mineralization in the southern Panagyurishte district, Srednogie zone, Bulgaria. In: Eliopoulos, D.G. (Ed.), *Mineral Exploration and Sustainable Development*. Millpress, Rotterdam, pp. 1181–1184.
- Lang, J.R., Baker, T., 2001. Intrusion-related gold systems: the present level of understanding. *Miner. Deposita* 36, 477–489.
- Large, R., Huston, D., McGoldrich, P., McArthur, G., Ruxton, P., 1988. Gold distribution and genesis in Paleozoic volcanogenic massive sulphide systems. *Abst. Ser. 22 In: Bicentennial Gold 88*. Geol. Soc. Aust., pp. 121–126.
- Lescuyer, J.L., Houshmandzadeh, A., Daliran, F., 2003. Gold metallogeny in Iran: a preliminary review. In: Eliopoulos, D.G. (Ed.), *Mineral Exploration and Sustainable Development*. Millpress, Rotterdam, pp. 1185–1188.
- Lowenstern, J.B., 2001. Carbon dioxide in magmas and implications for hydrothermal systems. *Miner. Deposita* 36, 490–502.
- Ludwig, K.R., 2003. User's Manual for Isoplot/Ex rev. 3.00; A Geochronological Toolkit for Microsoft Excel. Geochronology Center, Berkeley.
- Marsh, E.E., Goldfarb, R.J., Hart, C.J.R., Johnson, C.A., 2003. Geology and geochemistry of the Clear Creek intrusion-related gold occurrences, Tintina Gold Province, Yukon, Canada. *Can. J. Earth Sci.* 40, 681–689.
- Moore, J.M., 1979. Tectonics of the Najd transcurrent fault system, Saudi Arabia. *J. Geol. Soc. Lond.* 136, 441–454.
- Moradi, S., 2010. Investigation of Gold Mineralization in the Baghu Area, Southeast of Damghan (M.Sc. thesis). Damghan University, Damghan, pp. 224.
- Morávek, P., 1995. The Mokrosko gold deposit. In: Morávek, P. (Ed.), *Gold Deposit of the Central and SW Part of the Bohemian Massif*. Czech. Geol. Surv., Prague, pp. 33–61.
- Moritz, R., Jackquat, S., Chambeffort, I., Fontignie, D., 2003. Controls on ore formation at high sulfidation Au–Cu Chelopech deposit, Bulgaria: evidence from infrared fluid inclusion microthermometry of enargite and isotope systematics of barite. In: Eliopoulos, D.G. (Ed.), *Mineral Exploration and Sustainable Development*. Millpress, Rotterdam, pp. 1209–1212.
- Ohmoto, H., Rye, R.O., 1979. Isotopes of sulfur and carbon. In: Barnes, H.L. (Ed.), *Geochemistry of Hydrothermal Ore Deposits*. Wiley, New York, pp. 509–567.
- Omrani, J., 2008. The Geodynamic Evolution of Zagros: Tectonic and Petrological Constraints from Internal Zones (Ph.D. thesis). University of Paris, Paris, pp. 343.
- Paces, J.B., Miller, J.D., 1993. Precise U–Pb ages of the Duluth complex and related mafic intrusions, Northeastern Minnesota: geochronological insights to physical, petrogenetic, paleomagnetic, and tectonomagmatic processes associated with the 1.1 Ga midcontinent rift system. *J. Geophys. Res.* 98, 13997–14013.
- Pearce, J.A., Peate, D.W., 1995. Tectonic implications of the composition of volcanic arc magmas. *Annu. Rev. Earth. Pl. Sci.* 23, 251–285.
- Qi, L., Hu, J., Gregoire, D.C., 2000. Determination of trace elements in granites by inductively coupled plasma mass spectrometry. *Talanta* 51, 507–513.
- Quidelleur, X., Grove, M., Lovera, O.M., Harrison, T.M., Yin, A., Ryerson, F.J., 1997. Thermal evolution and slip history of the Renbu-Zedong thrust, southeastern Tibet. *J. Geophys. Res.* 102, 2659–2679.
- Rahmati-Ilkhchi, M., Jerabek, P., Faryad, S.W., Koyi, H.A., 2010. Mid-Cimmerian, Early Alpine and Late Cenozoic orogenic events in the Shotor Kuh metamorphic complex, Great Kavir block, NE Iran. *Tectonophysics* 494, 101–117.
- Rashidinejad-Omrani, N., 1992. The Study of Magmatic Evolution in the Baghu Area and Relation with Gold Mineralization, SE Damghan (M.Sc. thesis). University of Tarbiat Moaleem, Tehran, pp. 324.
- Rastad, E., Fard, M., Rashidinejad-Omrani, N., Ghaderi, M., 1999. Mineralization and potential of gold in Torud-Chahshirin volcano-plutonic complex (south Damghan) [abs.]. Abstracts with Programs 5. Geol. Soc. Iran, pp. A214–A215.
- Richards, J.P., Spell, T., Rameh, E., Raziqee, A., Fletcher, T., 2012. High Sr/Y magmas reflect arc maturity, high magmatic water content, and porphyry Cu  $\pm$  Mo  $\pm$  Au potential: Examples from the Tethyan arcs of central and eastern Iran and western Pakistan. *Econ. Geol.* 107, 295–332.
- Riedel, W., 1929. Zur Mechanik geologischer Brucherscheinungen. *Zentralbl. Mineral.* Abt. 2, 354–368.
- Roedder, E., 1984. Fluid Inclusions. Reviews in Mineralogy. Mineral. Soc. Am., Washington.
- Rossetti, F., Nasrabad, M., Vignaroli, G., Theye, T., Gerdes, A., Razavi, M., Moin, Vaziri, H., 2010. Early Cretaceous migmatitic mafic granulites from the Sabzevar range (NE Iran): implications for the closure of the Mesozoic peri-Tethyan oceans in central Iran. *Terra Nova* 22, 26–34.
- Rye, R.O., 1993. The evolution of magmatic fluids in the epithermal environment: the stable isotope perspective. *Econ. Geol.* 88, 733–753.
- Sahandi, M.R., Sohili, M., 2014. Geological Map of Iran (GSI based) Scale 1:1,000,000. Geol. Surv. Iran, Tehran.
- Sanchez, M.G., Bissig, T., Kowalczyk, P., 2015. Toward an improved basis for beneath cover mineral exploration in the QUEST area, central British Columbia: new structural interpretation of geophysical and geological datasets (NTS 093A, B, G, H, J, K, N). In: Sanchez, M.G. (Ed.), *Geosciences British Columbia Reports*. Nat. Resour., Can. Victoria, pp. 53–62.
- Sanudo-Wilhelmy, S.A., Flegal, A.R., 1994. Temporal variations in lead concentrations and isotopic composition in the Southern California. *Geochim. Cosmochim. Acta* 58, 3315–3320.
- Schmitt, A.K., Grove, M., Harrison, T.M., Lovera, O., Hulen, J.B., Walters, M., 2003a. The Geysers-Cobb mountain magma system California (Part 1): U–Pb zircon ages of volcanic rocks conditions of zircon crystallization and magma residence times. *Geochim. Cosmochim. Acta* 67, 3423–3442.
- Schmitt, A.K., Grove, M., Harrison, T.M., Lovera, O., Hulen, J.B., Walters, M., 2003b. The Geysers-Cobb mountain magma system California (Part 2): timescales of pluton emplacement and implications for its thermal history. *Geochim. Cosmochim. Acta* 67, 3443–3458.
- Seal, R.R., 2006. Sulfur isotope geochemistry of sulfide minerals. *Rev. Mineral. Geochem.* 61, 633–677.
- Shamarian, G.H., Hedenquist, J.W., Hattori, H., Hassanzadeh, J., 2004. The Gandy and Abolhassani epithermal prospects in the Alborz magmatic Arc, Semnan province, northern Iran. *Econ. Geol.* 99, 691–712.
- Shaykhi, H., 2013. Geology, alteration and gold genesis in Baghu deposit, Damghan. (M. Sc. thesis) Damghan University, Damghan, (187 pp.).
- Shepherd, T.J., Rankin, A.H., Alderton, D.H.M., 1985. A practical guide to fluid inclusion studies. Blackie, Glasgow.
- Shojaat, B., Hassanipak, A.A., Mubasher, K., Ghazi, A.M., 2002. Petrology, geochemistry and tectonics of the Sabzevar ophiolite, North Central Iran. *J. Asian Earth Sci.* 21, 1053–1067.
- Sillitoe, R.H., 2008. Major gold deposits and belts of the North and South American Cordillera: distribution, tectonomagmatic settings, and metallogenic considerations. *Econ. Geol.* 103, 663–687.
- Sillitoe, R.H., Thompson, J.F.H., 1998. Intrusion-related gold deposits: types, tectonomagmatic settings and difficulties of distinction from orogenic gold deposits. *Resour. Geol.* 48, 237–250.
- Spiridonov, E.M., 1996. Granitic rocks and gold mineralization of North Kazakhstan. In: Shatov, V., Seltmann, R., Kremenetsky, A., Lehmann, B., Popov, V., Ermolov, P. (Eds.), *Granite-Related Ore Deposits of Central Kazakhstan and Adjacent Areas*. Glagol. Publishing House, Saint Petersburg, pp. 197–217.
- Stacey, J.C., Kramers, J.D., 1975. Approximation of terrestrial lead isotope evolution by a two-stage model. *Earth Planet. Sci. Lett.* 26, 207–221.
- Stampfli, G.M., Borel, G.D., 2002. A plate tectonic model for the Paleozoic and Mesozoic constrained by dynamic plate boundaries and restored synthetic oceanic isochrones. *Earth Planet. Sci. Lett.* 196, 17–33.
- Stephens, J.R., Mari, J.L., Oliver, N.H.S., Hart, C.J.R., Baker, T., 2004. Structural and mechanical controls on intrusion-related deposits of the Tombstone Gold Belt, Yukon, Canada, with comparisons to other vein-hosted ore-deposit types. *J. Struct. Geol.* 26, 1025–1041.
- Sterner, S.M., Bodnar, R.J., 1984. Synthetic fluid inclusions in natural quartz. I. Types and applications to experimental geochemistry. *Geochim. Cosmochim. Acta* 48, 2659–2668.
- Stöcklin, J., 1968. Structural history and tectonics of Iran, a review. *Am. Assoc. Petr. Geol. B.* 52, 1229–1258.
- Sun, S.S., McDonough, W.F., 1989. Chemical and isotopic systematics of oceanic basalts: implications for mantle composition and processes. In: Saunders, A.D., Norry, M.J. (Eds.), *Magmatism in the Ocean Basins*. Geol. Soc. Lond., pp. 313–345.
- Taghipour, B., Mackizadeh, M., 2014. The origin of the tourmaline-turquoise association hosted in hydrothermally altered rocks of the Kuh-Zar Cu–Au-turquoise deposit, Damghan, Iran. *Neues Jahrb. Mineral. Abh.* 272, 61–77.
- Tajeddin, H., 1999. Geology, Mineralogy, Geochemistry and Genesis of Darestan Gold Occurrences, South Damghan (M.Sc. thesis). Tarbiat Modarres University, Tehran, pp. 236.
- Takin, M., 1972. Iranian geology and continental drift in the Middle East. *Nature* 23, 147–150.
- Thompson, J.F.H., Sillitoe, R.H., Baker, T., Lang, J.R., Mortensen, J.K., 1999. Intrusion-related gold deposits associated with tungsten-tin provinces. *Mineral. Deposita* 34, 323–334.
- Touret, J., Dietvorst, P., 1983. Fluid inclusions in high-grade anatectic metamorphites. *J. Geol. Soc. London* 140, 635–649.
- Ulrich, T., Gunther, D., Heinrich, C., 2001. The evolution of a porphyry Cu–Au deposit based on LA-ICPMS analysis of fluid inclusions: Bajo de Alumbrera, Argentina. *Econ. Geol.* 96, 1743–1774.
- Verdel, C., Wernicke, B.P., Hassanzadeh, J., Guest, B., 2011. A Paleogene extensional arc flare-up in Iran. *Tectonics* 30, 1–20.
- Volkov, A.V., Savva, N.E., Sidorov, A.A., Prokofev, V.Y., Goryachev, N.A., Voznesensky, S.D., Al'Shevsky, A.V., Chernova, A.D., 2011. Shkol'noe gold deposit, the Russian Northeast. *Geol. Ore. Deposit.* 53, 1–26.
- Wallace, P.J., Edmonds, M., 2011. The sulfur budget in magmas: evidence from melt inclusions, submarine glasses, and volcanic gas emissions. *Rev. Mineral. Geochem.* 73, 215–246.
- Weis, P., 2015. The dynamic interplay between saline fluid flow and rock permeability in magmatic-hydrothermal systems. *Geofluids* 15, 350–371.
- Williams-Jones, A.E., Heinrich, C., 2005. Vapor transport of metals and the formation of magmatic-hydrothermal ore deposits. *Econ. Geol.* 100, 1287–1312.
- Xiong, X.L., Xia, B., Xu, J.F., Niu, H.C., Xiao, W.S., 2006. Na depletion in modern adakites via melt/rock reaction within the sub-arc mantle. *Chem. Geol.* 229, 273–329.
- Yang, X.M., 2012. Sulphur solubility in felsic magmas: implications for genesis of intrusion-related gold mineralization. *Geosci. Can.* 39, 17–32.
- Yilmaz, A., Yilmaz, H., Kaya, C., Boztu, G.D., 2010. The nature of the crustal structure of the eastern Anatolian Plateau. *Turkey. Geodin. Acta* 23, 167–183.
- Yilmaz, H., 2007. Stream sediment geochemical exploration for gold in the Kazdag Dome in the Biga Peninsula, western Turkey. *Turk. J. Earth. Sci.* 16, 33–35.
- Zhang, Y., Frantz, J.D., 1987. Determination of the homogenization temperatures and densities of supercritical fluids in the system NaCl–KCl–CaCl<sub>2</sub>–H<sub>2</sub>O using synthetic fluid inclusions. *Chem. Geol.* 64, 335–350.
- Zheng, Y., 1993. Calculation of oxygen isotope fractionation in anhydrous silicate minerals. *Geochim. Cosmochim. Acta* 57, 1079–1091.